nature communications

Article

https://doi.org/10.1038/s41467-025-61434-5

Unlocking tumor barrier: annexin A2-mediated transcytosis boosts drug delivery in pancreatic and breast tumors

Received: 25 February 2025

Accepted: 17 June 2025

Published online: 15 July 2025

Check for updates

Yanyan Liu[1,7], Qikai Wang[1,2,7], Zhenhan Feng[1,2,7], Mengmeng Qin[1,7], Zhenyu Zhang[1,2], Jinhong Jiang[3], Tongxiang Ren[4], Xiangsheng Liu[3], C. Jeffrey Brinker[5], Yuliang Zhao[1,6] & Huan Meng[1]

The efficacy of many cancer nanocarriers has traditionally been attributed to enlarged tumor vasculature fenestrations, giving rise to the concept of the enhanced permeability and retention (EPR) effect. However, emerging evidence suggests that active biological processes, such as transcytosis, may play a central (and sometimes dominant) role in nanoparticle transport across tumor vasculature. In this study, we develop lipid-coated mesoporous silica nanoparticles (LC-MSNP) as a model platform to investigate the contribution of surface-bound proteins to transcytosis-mediated tumor delivery. Through comparative analysis, we identify Annexin A2 (A2) as a key endogenous protein that facilitates this process. Pre-coating LC-MSNP with A2 significantly enhances the delivery of irinotecan and doxorubicin to breast and pancreatic tumors in vivo. This strategy is successfully extended to both an in-house liposome formulation and a commercial doxorubicin liposome, leading to improved therapeutic efficacy, including long-term survival in a subset of treated mice. Mechanistic studies reveal that this enhancement is governed by a specific nanosurface-A2-α5β1 integrin interaction. In both murine and patient-derived xenograft models, therapeutic benefit correlates with α5β1 integrin expression on tumor vasculature. These findings establish a mechanistic basis for protein-mediated transcytosis and provide a translational strategy to improve the performance of clinically approved nanomedicines.

There has been significant debate and new insight regarding the accurate interpretation of the "enhanced permeability retention" (EPR) effect, which enables cancer nanocarriers to penetrate solid tumors[1–7]. In contrast to the traditional explanation of EPR effect, which primarily attributes tumor vasculature leakiness as the main factor governing nanoparticle delivery/accumulation, recent evidence, including our own data, has shed light on the significant role of "transcytosis", particularly in stroma-rich solid tumors such as pancreatic cancer (PDAC) and breast cancer (BC)[8–10]. For example, scientists have identified a specific sub-population of $CD31^{+}CD45^{-}$ endothelial cells (EC) at the

[1]CAS Key Laboratory for Biomedical Effects of Nanomaterials and Nanosafety, National Center for Nanoscience and Technology, Beijing, China. [2]University of Chinese Academy of Sciences, Beijing, China. [3]Zhejiang Cancer Hospital, Hangzhou Institute of Medicine (HIM), Chinese Academy of Sciences, Hangzhou, China. [4]National Institute of Metrology of China, Beijing, China. [5]The University of New Mexico, Center for Micro-Engineering Materials, Albuquerque, US. [6]College of Chemistry and Materials Science, and Institute of Nanotechnology and Intelligence (INAI), Jinan University, Guangzhou, China. [7]These authors contributed equally: Yanyan Liu, Qikai Wang, Zhenhan Feng, Mengmeng Qin. e-mail: mengh@nanoctr.cn

tumor site, which has been shown to govern over 97% of nanoparticle tumor access in the 4T1 orthotopic BC model[4]. Additionally, achieving efficient intratumoral distribution of nanocarriers was possible by utilizing cationic nanocarrier transcytosis among cancer cells. The latter mechanism allows nanocarriers to traverse through cancer cells, facilitating their widespread distribution within the tumor[6]. In the case of fucoidan nanoparticle, the researchers demonstrated that P-selectin facilitated nanomaterial trans-EC transport across blood-brain barrier (BBB) via caveolin-1-mediated transcytosis[11]. These mechanisms are collectively described by the active transport and retention (ATR) principle, which posits that nanoparticles primarily enter tumors via active transport processes—such as transcytosis, vesiculo-vacuolar organelles (VVO), and immune cell migration—rather than through enlarged EC fenestration[12].

While there is now recognition of the limited EPR effect in PDAC[3,13,14] and BC[4,15], the currently prescribed nanoformulations for these cancers, including irinotecan (IRIN) and doxorubicin (DOX)-loaded liposomes, were not intentionally designed to address the challenges posed by tumor EC. Instead, these liposomes seem to rely on the putative EPR effect, which may not always be present or efficient in PDAC and BC, to say the least. Therefore, there is an urgent need for an efficient approach to enhance the performance of nanocarriers in cancer types with a poor EPR effect. This includes the consideration of using activated transcytosis[14] (among other methods) to allow nanocarriers tumor access, irrespective of the EC leakiness[8,16,17]. Previous studies involved the therapeutic utilization of the iRGD peptide, which triggers NRP-1-mediated transcytosis of nanocarriers[3,10,18]. A second approach involves the introduction of a cationic charge[6], which promotes transcytosis from the peri-EC region to the tumor's interior. While encouraging, further studies are needed to assess whether the released payload impacts transcytosis efficiency. A third option utilizes surface-conjugated modification such as transferrin[19–22]. This recognition leads to the initiation of receptor-mediated transcytosis, particularly in the context of BBB[23]. Moreover, various imaging modalities were used to predict the effectiveness of EPR or ATR mechanisms. For example, magnetic resonance imaging (MRI) and computed tomography-fluorescence molecular tomography (CT-FMT) have been employed to assess EPR, while immunohistochemistry (IHC) and immunofluorescence (IF) staining of NRP-1 can predict iRGD-mediated transcytosis[3,24,25].

In this investigation, we employ a series of imageable lipid-coated mesoporous silica nanoparticles (LC-MSNP)[26,27] as "model nanoparticles" to identify the composition of the protein attachment on the nanoparticle surface. This analysis reveals the presence of proteins from the Annexin family, notably Annexin A2 (A2), which plays a key role during transcytosis[28,29]. When A2 is deliberately introduced to the LC-MSNP's surface, we observe a significant improvement in the ability of these nanocarriers to access tumors and in drug delivery performance in mice with PDAC and BC via a transcytosis-mediated mechanism. Efficacy improvement through transcytosis is first seen with IRIN- and DOX-loaded LC-MSNPs, and later in in-house liposomes. After analyzing PEGylation, size, and physiological factors, we prioritize in vivo testing of a PEGylated commercial DOX liposome for BC. A2 enhances the efficacy of this commercial liposome and leads to long-term survival in 2 out of 8 mice. Computational modeling shows that A2's effect relies on interaction among nanosurface-A2-α5β1 integrin. In a murine BC model, A2's effect correlates with α5β1 expression on tumor blood vessels, which is further confirmed in patient-derived xenografts (PDX) with high α5β1 integrin expression.

Results

Comparison of the biodistribution of charge-designed LC-MSNPs in tumor-bearing mice

We have previously demonstrated that intravenously injected (IV) LC-MSNP can enter a KPC-derived orthotopic PDAC model, partially via a transcytosis-mediated mechanism[3] (Fig. 1a). Based on this knowledge, our primary objective was to investigate how the design of the particle lipid coating impacts the abundance and mechanism of tumor biodistribution in PDAC. We favor LC-MSNP as a "model nanoparticle" due to the ease of particle visualization and the flexibility it offers for tuning lipid composition. Additionally, it enables the potential to leverage data generation using LC-MSNP for non-supported bilayers, which could enhance the performance of liposomes, under certain conditions (a topic to be discussed later). For the biodistribution study, we utilized KPC cells derived from a spontaneous PDAC tumor in a transgenic *Kras*$^{LSL\text{-}G12D/+}$*Trp53*$^{LSL\text{-}R172H/+}$*Pdx1-Cre* mouse[30]. This stroma-rich, stringent PDAC tumor model closely mimics human PDAC in terms of oncogene expression, growth characteristics, metastasis, histological features, and development of a dysplastic stroma, as evidenced by robust tumor growth and trichrome staining (Fig. 1b).

Three types of LC-MSNPs (designated F1-F3) were developed (Fig. 1c). Bare MSNPs (~70 nm) were synthesized using a sol-gel method[31,32] and subsequently coated using our published ethanol exchange technique with different lipid mixtures[9]. The lipid coatings were comprised of DSPC:DOPA:DOTAP:Chol:DSPE-PEG$_{2000}$ at the indicated molar ratios (Fig. 1c). To visualize the nanoparticles in vivo, our LC-MSNPs were designed to incorporate 0.1 wt% near-infrared (NIR) dye, Dylight 680 (Dy680). The resulting nanoparticles exhibited similar morphologies but distinct surface charges, with zeta potential values of −6.6 ± 1.3 mV (F1, close to neutral, capable of transcytosing through EC barriers)[3], −26.0 ± 2.8 mV (F2, strongly negative), and +16.2 ± 2.2 mV (F3, positive). Orthotopic KPC tumor mice were then IV injected with 50 mg/kg of each NIR dye-labeled LC-MSNPs. After 24 h post-IV injection, the mice were sacrificed, and the tumor and major organs, such as the liver and spleen, were visualized using IVIS imaging. The signal intensities were subsequently quantified using the IVIS software (Fig. 1d, left panel). Our analysis revealed the highest particle signal at the tumor site in animals treated with F1 (Fig. 1d). In contrast, F2 and F3 led to relatively low tumor accumulation, and F2 exhibited a trend of enhanced uptake in the liver.

Identification of surface-attached proteins on F1-F3 nanoparticles

In light of the biodistribution data, we investigated the potential role of surface-attached proteins in terms of abundance and the mechanism of nanoparticle tumor access, with a specific focus on transcytotic delivery. Accordingly, we conducted an abiotic study by mixing various nanoparticles with mouse serum obtained from KPC orthotopic tumor-bearing mice. We prioritized the analysis of protein components due to their stability during circulation and potential as a means to enhance nanocarrier tumor accessibility. Accordingly, we removed associated or loosely attached proteins following published protocols[33,34] (Fig. 2a). Mass spectrum analysis allowed us to identify a total of 46 proteins for F1 ~ F3 samples (Fig. 2b). Noteworthy, we paid attention to F1-only protein types (zone α in Fig. 2b, lower panel) and the top proteins that were common across all three particle types (zone β in Fig. 2b). By searching the UniProt website, we have identified two intriguing targets, B0V2N8 in zone α (correlating with Annexin fragment) and P29788 in zone β (correlating with Vitronectin fragment) (Fig. 2c). The former is interesting because an Annexin subtype was previously reported in transcytosis-mediated transportation of peptide-conjugated chemotherapeutics across the BBB[35]. Vitronectin (VTN) is interesting because it interacts with integrin, an important receptor on EC surface during transcytosis[36,37]. This informative dataset prompted us to acquire recombinant Annexin proteins, including A2, A3, A5, A7, and A8, along with VTN (Fig. 2d, right panel). Additionally, we also obtained albumin and GAPDH as controls. Subsequently, we incubated these individual pure proteins with F1 sample for 1 hour, after which we collected the particle-protein complexes for protein extraction and electrophoresis analysis (Fig. 2d, left panel). We

https://doi.org/10.1038/s41467-025-61434-5

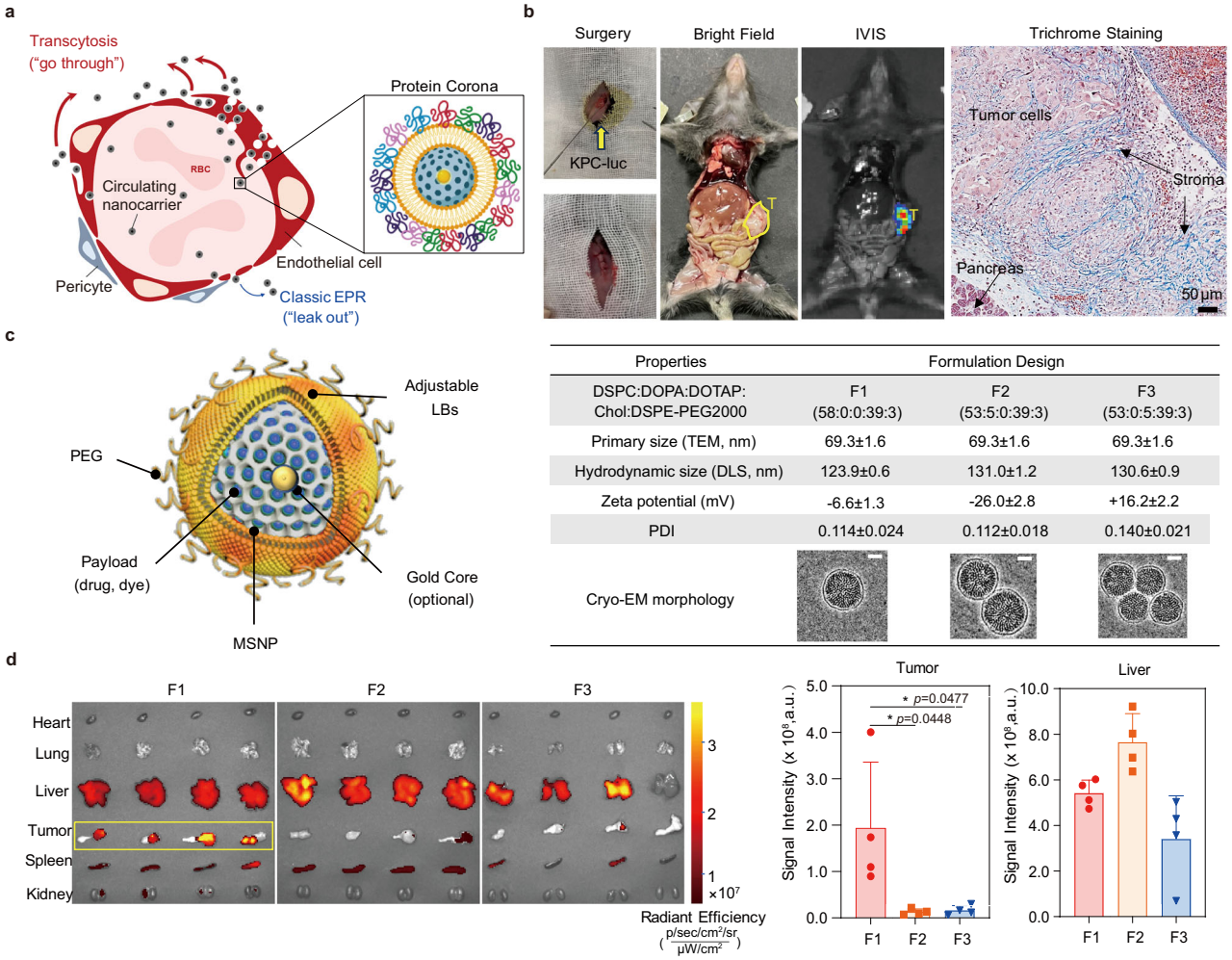

Properties	Formulation Design		
DSPC:DOPA:DOTAP: Chol:DSPE-PEG2000	F1 (58:0:0:39:3)	F2 (53:5:0:39:3)	F3 (53:0:5:39:3)
Primary size (TEM, nm)	69.3±1.6	69.3±1.6	69.3±1.6
Hydrodynamic size (DLS, nm)	123.9±0.6	131.0±1.2	130.6±0.9
Zeta potential (mV)	-6.6±1.3	-26.0±2.8	+16.2±2.2
PDI	0.114±0.024	0.112±0.018	0.140±0.021
Cryo-EM morphology			

Fig. 1 | Comparative biodistribution profiles of IV-injected LC-MSNPs in KPC-luc orthotopic PDAC model. a We engineered LC-MSNPs with distinct lipid compositions, yielding particles with negative, close to neutral, and positive surface charges. This design facilitated a comprehensive analysis of surface protein binding, shedding light on the mechanisms governing nanoparticle tumor access (*Created in BioRender. Meng, H. (2025)* https://BioRender.com/24rk3w2). **b** We established an orthotopic KPC model, a stringent preclinical model for studying drug delivery. Luciferase genes were introduced into KPC cells. After the orthotopic implantation of KPC-luc cells, subsequent autopsy and bioluminescence imaging uncovered primary tumor growth within 1 ~ 2 weeks. Trichrome staining showed a stroma-rich primary tumor adjacent to normal pancreas tissue ($n = 3$ independent experiments). **c** Our study included three LC-MSNP variants: F1 ~ F3. The table summarizes the physicochemical properties of F1 ~ F3 samples. Scale bar = 35 nm. **d** We present ex vivo IVIS imaging of tumor-bearing mice that received IV DyLight 680-labeled F1-F3 at 50 mg/kg ($n = 4$ mice). Tumor tissue and major organs were harvested 24 h post-injection. Fluorescence intensity was quantified in the tumor and liver, utilizing the IVIS living image software for region-of-interest (ROI) analysis. Notably, F1 gave the highest particle signal at the tumor site. Data are depicted as mean ± SD. Statistical significance was evaluated through two-tailed unpaired t-tests. Source data are provided as a Source Data file.

were able to confirm the robust binding of Annexin proteins, particularly A2 and A5, as well as VTN, showing relatively high abundance in the protein coat formed on the F1 nanoparticle surface.

Annexin A2 pre-coating improves nanoparticle tumor access via a transcytosis-mediated mechanism

We have identified and validated the presence of Annexin proteins and VTN on the F1 nanoparticle, which was the best-performing particle for KPC tumor access. Subsequently, we explored whether protein pre-coating could improve biodistribution. To investigate this, we created a series of nanocarriers by utilizing F1 nanoparticles with or without protein coatings. Prior to in vivo testing of protein-coated particles, we employed an EC transwell setup to assess the potential of nanoparticle transcytosis across HUVEC monolayers (Fig. 3a, left panel). The results demonstrated a substantial enhancement in the transportation of nanoparticles pre-coated with A2, A3, A5 and VTN through EC cells (Fig. 3a, right panel). The consistency of the EC monolayer integrity, confirmed by the FITC-dextran assay (Fig. S1), underscores the accuracy of the observed differences in transcytosis induced by various surface pre-coating. While promising, a limitation of the transwell study was the use of fetal bovine serum-supplemented complete DMEM (CDMEM), which led to a high PDI value during dynamic light scattering (DLS) analysis. For instance, A2-coated F1 nanoparticles had a size of 140.1 ± 2.5 nm and a PDI of 0.292 in CDMEM. Systemic analysis using PBS, CDMEM, and serum-supplemented saline (mimicking the bloodstream in vivo) showed that the increased PDI occurred only in CDMEM. In PBS, A2-coated F1 nanoparticles measured 135.8 ± 4.6 nm with PDI = 0.131, and in serum-supplemented saline, they were 134.2 ± 2.1 nm with PDI = 0.108 (Table S1). Nevertheless, we further tested the coating effect of A2, A5, and VTN in vivo. We chose not to pursue A3 due to its inaccessibility, as well as previous studies indicating its potential to exacerbate the invasiveness of cancer[38].

Accordingly, we IV injected A2-coated Dy680-labeled F1 particles into mice with orthotopic KPC tumor. We sacrificed the animals after 24 h and performed ex vivo IVIS imaging of explanted tumors and major organs, such as heart, lung, liver, spleen and kidney.

https://doi.org/10.1038/s41467-025-61434-5

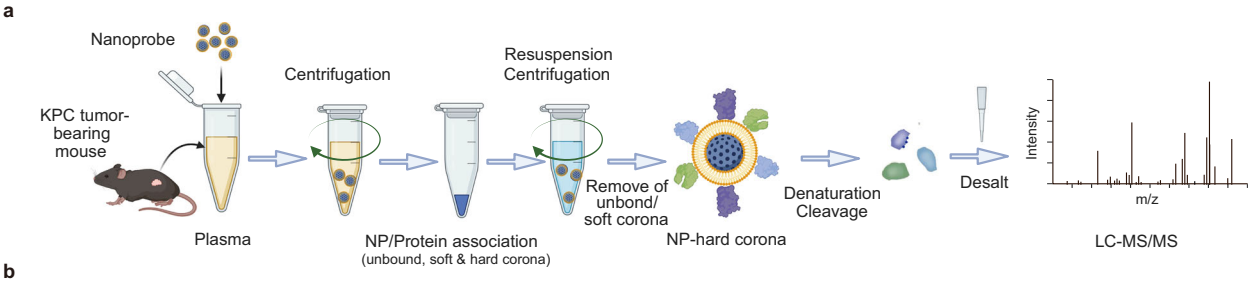

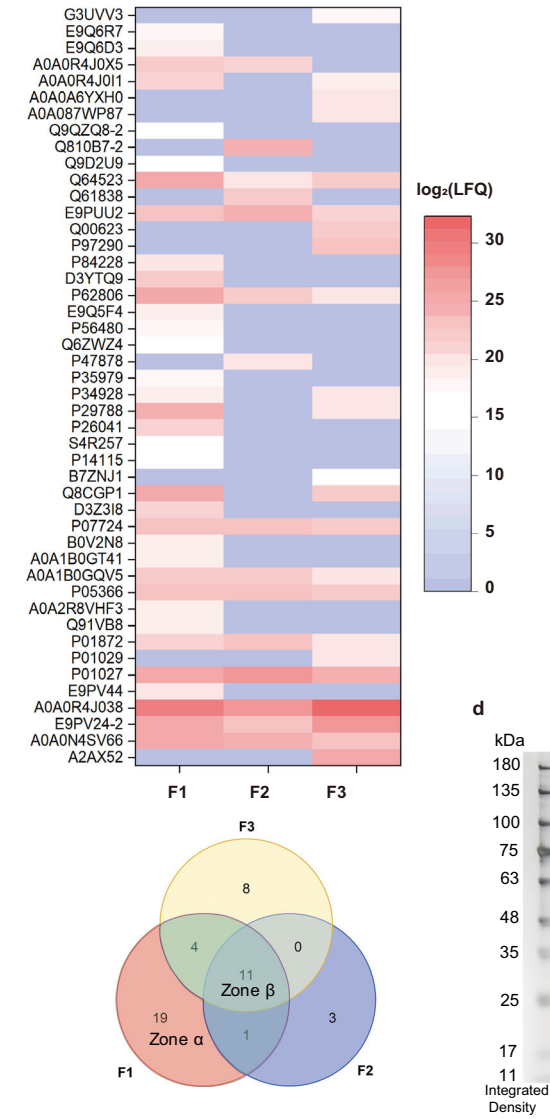

c

No	Protein ID	Protein Name	Function	Abundance
Zone α				
1	D3YTQ9	40S ribosomal protein S15	Constitute ribosomal	22.2
2	P26041	Moesin	Connects actin cytoskeleton	21.2
3	D3Z3I8	Elongation factor 1alpha 1	Promotes the binding of aminoacyl - tRNA	20.8
4	P84228	Histone H3.2	Core component of nucleosome	20.3
5	E9PV44	ATP synthase F1 subunit epsilon	Mitochondrial enzyme	19.7
6	A0A2R8VHF3	Tubulin alpha chain	Major constituent of microtubules	19.1
7	B0V2N8	Annexin (Fragment)	Transcytosis	19.1
8	E9Q5F4	Actin, cytoplasmic 1	Cytoplasmic cytoskeleton	18.9
9	Q91VB8	Alpha globin 1	Oxygen transport	18.9
10	A0A1B0GT41	L-lactate dehydrogenase A chain	Catalyzes lactate to pyruvate	18.8

No	Protein ID	Protein Name	Function	Abundance
Zone β				
1	A0A0R4J038	Bradykinin	Regulate smooth muscle	30.1
2	P62806	Histone H4	Nucleosome component	25.7
3	A0A0N4SV66	Histone H2A	Nucleosome component	25.6
4	Q64523	Histone H2A type 2-C	Nucleosome component	25.5
5	E9PV24-2	Isoform 2 of Fibrinogen alpha chain	Cleaved by thrombin	25.3
6	Q8CGP1	Histone H2B type 1-K	Transcription	25.0
7	P01027	Complement C3	Activation of the complement	24.8
8	P29788	Vitronectin	Bind to integrins	24.3

d

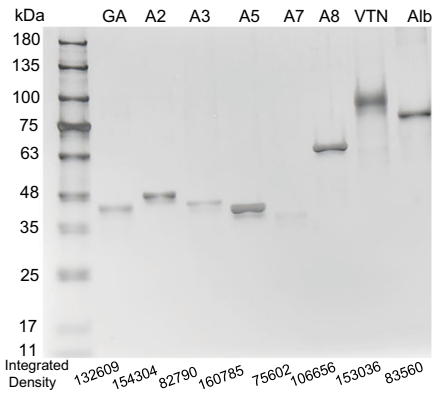

Protein type	MW (kDa)	pI value
GAPDH	36	~8.5
ANX A2	39	7.57
ANX A3	36	5.6
ANX A5	36	4.9
ANX A7	34	5.9
ANX A8	37	5.6
VTN	80	~5
Albumin	67	4.7

Fig. 2 | Identification of key surface-attached protein species in relation to nanocarrier transcytosis. a To understand the role of protein attachment on biodistribution, we gathered serum from KPC tumor-bearing mice. Subsequently, various particle variants, F1 to F3, were subjected to serum incubation, followed by mass spectrometry analysis, as outlined in the schematic (*Created in BioRender. Meng, H. (2025)* https://BioRender.com/ffbjjg3). **b** A heat map showed the most abundant proteins detected on the surfaces of the nanocarriers. We present the 46 proteins exhibiting high abundance. The lower panel is the Venn diagram of identified proteins across F1 - F3. The distinct protein species unique to the best-performing particle (F1) during the biodistribution study are highlighted by the α zone (in red). The β zone (in cyan) included protein types detected in F1, which also appeared in F2 and F3. **c** Using UniProt database, detailed protein functions for the most abundant proteins in zone α (upper part) and zone β (lower part) were provided. **d** Based on the findings from (**c**), we purchased ANX A2, ANX A3, ANX A5, ANX A7, and ANX A8. Pure VTN, albumin and GAPDH were also obtained. Following incubation of F1 particles with these protein types, an electrophoresis assay confirmed the efficient attachment of these proteins to F1 ($n = 3$ independent experiments). Source data are provided as a Source Data file.

We observed a moderate yet statistically significant (i.e., twofold) increase in KPC tumor signal for both the A2 and A5 groups compared to various controls. Interestingly, the A5 pre-coating, but not A2, resulted in an increased signal in the liver (Fig. 3b). Moreover, before further testing on A2, we also confirmed that A2 coating remained stable and unchanged for at least 48 h post-preparation (Table S2, Fig. S2).

Encouraged by the KPC data, we expanded our study to include additional stroma-rich syngeneic orthotopic tumor models, such as BC (4T1, EMT6, and PyMT-derived Py8119 models) and

https://doi.org/10.1038/s41467-025-61434-5

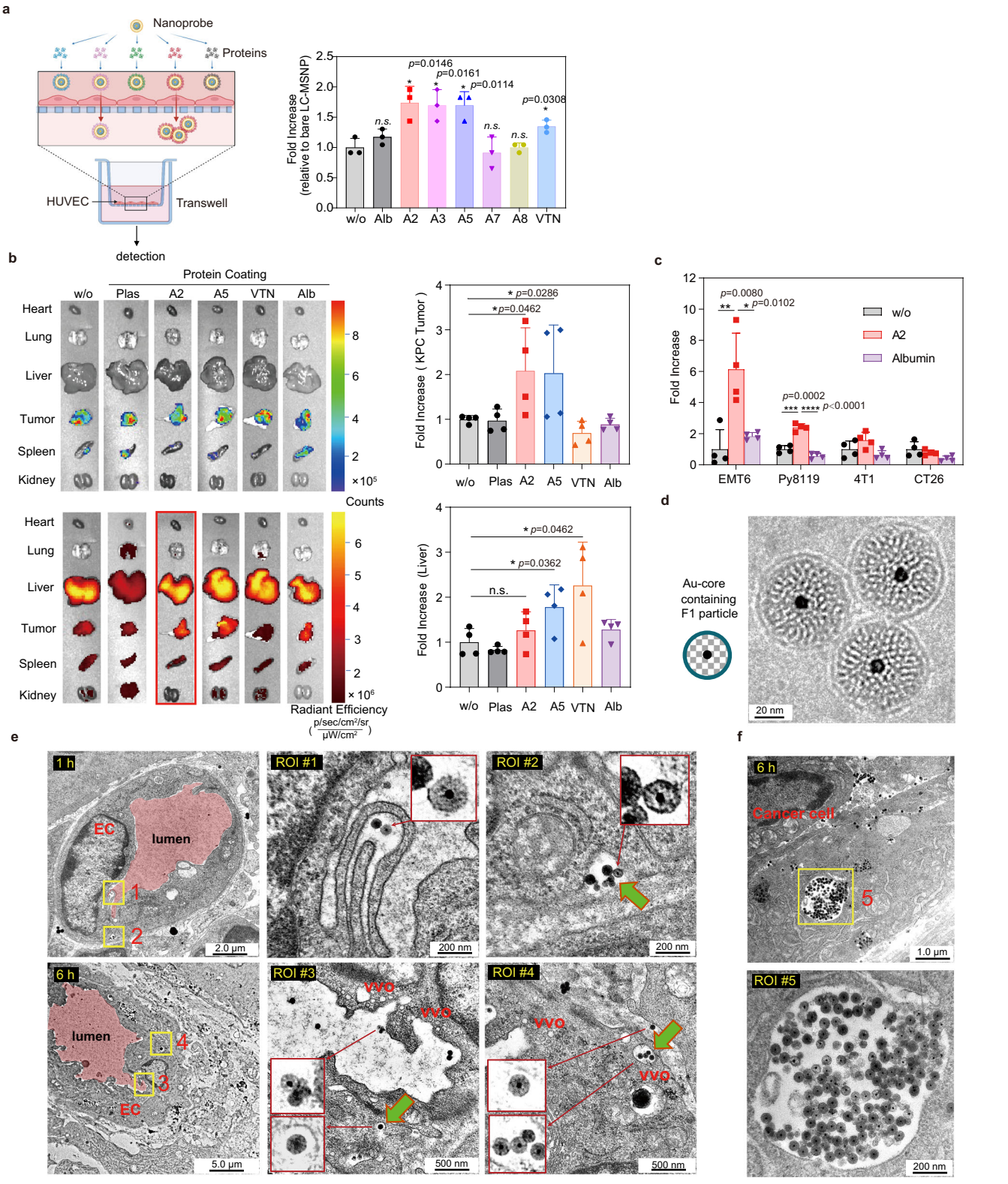

colon cancer (CT26). This allowed us to identify EMT6 BC, which exhibited a remarkable sixfold increase after a single injection in tumor signal using A2 pre-coating (Figs. 3c and S3–4). This could be substantial for preclinical anti-cancer efficacy studies, which typically require about 4 - 10 IV administrations in mice. The Py8119 orthotopic model also demonstrated an approximate 2-fold increase. 4T1 and CT26 tumors showed minimal response to the treatment; the underlying mechanisms behind the low response in these models are likely complex and require independent investigation in the future.

Transmission electron microscopy (TEM), capable of revealing morphological characteristics of nanoparticle transcytosis, was utilized to demonstrate this intriguing phenomenon at an ultrastructural level, at 1 and 6 h after IV injection in KPC orthotopic tumors. Here, we replicated the A2 coating experiment using an alternative version of the F1 particle, featuring a 10 nm gold core while preserving identical

Fig. 3 | Augmented tumor access of LC-MSNP via A2 pre-coating and transcytosis-mediated mechanism. a The impact of protein pre-coating on nanocarrier transcytosis activity was studied using a transwell assay, wherein enhanced transcytosis activity of A2, A3, A5 and VTN pre-coating compared with albumin pre-coating particles and non-coated LC-MSNP ($n = 3$ independent experiments, two-tailed unpaired t test) (*Created in BioRender. Meng, H. (2025)* https://BioRender.com/bnpp34l). **b** IVIS imaging revealed the biodistribution within the tumor and major organs ($n = 4$ mice, two-tailed unpaired t test). Semi-quantification of fluorescent intensity unveiled a ~2-fold enrichment in KPC tumor distribution in the A2 coating group, without disrupting biodistribution in other organs. **c** The A2 coating approach was replicated in additional orthotopic models, namely breast cancer (EMT6, Py8119, and 4T1) and colon cancer (CT26) ($n = 4$ mice, two-tailed unpaired t test). Encouragingly, ~6-fold improvement in tumor access was observed in the EMT6 BC model after a single IV injection. **d** A gold-core labeled version of F1, pre-coated with A2 protein, was prepared ($n = 3$ independent experiments). **e** Tumor samples were harvested at 1- and 6-hour post IV injection, followed by tumor tissue TEM study. EC endothelial cells, VVO vesiculo-vacuolar organelle. Inserted images confirmed the presence of gold labeling within the particles. Green arrows: Transcytosing nanoparticles inside EC vesicles ($n = 3$ independent experiments). **f** TEM image substantiated nanoparticle presence within a cancer cell 6 h post IV injection. Data are depicted as mean ± SD. Statistical significance was evaluated via two-tailed unpaired *t* test. Source data are provided as a Source Data file.

size and lipid coating. The morphology of as-prepared gold-containing F1 appeared in Fig. 3d. This modification addresses the challenge of low electron density observed with nano silica, enabling ready visualization within the heterogeneous tumor microenvironment. At 1 hour, we observed gold-labeled LC-MSNP model nanoparticles within the blood vessel lumen, the formation of filopodia (Fig. 3e, upper panel, ROI #1), and evidence of vesicular transport inside the ECs (Fig. 3e, upper panel, ROI #2). Similar observations were made at 6 h (Fig. 3e, lower panel, ROI #3), along with particle deposition within the tumor matrix (Fig. 3e, lower panel, ROI #4). Notably, at 6 h, we also identified A2-coated LC-MSNP displaying a perinuclear distribution within the cancer cell (Fig. 3f, ROI #5). Small insert boxes highlighted the gold labeling on the LC-MSNP model particles, enabling confident identification of the particle of interest at single-particle resolution. TEM pictures for control tumor and additional TEM evidence on A2-mediated transcytotic delivery appeared online (Fig. S5).

Biodistribution improvement was governed by nanosurface-A2-α5β1 integrin interactions

To investigate the role of A2 attachment on transcytosis activation, we first conducted molecular dynamics (MD) simulations to analyze the interactions between A2 and the lipid molecules. These lipid molecules, which mimic the lipid coat on MSNP, were designed based on the wet experiment. To save time and accommodate the complexity of the macromolecular system, we initially constructed the system's structure (Fig. 4a, left panel) using the Martini Force Field. This allowed us to obtain a well-equilibrated system (Fig. 4a, right panel). During the coarse-grained (CG) simulation, we observed the A2 protein reaching a stable position at the lipid membrane within 50 μs. We also calculated the root mean square deviation (RMSD) of the heavy atoms of the protein in relation to their initial positions, *i.e.*, 22 Å (Fig. 4b, upper panel). Subsequently, the CG final structure became the initial structure for the all-atom (AA) simulation, for 500 ns MD analysis. In this case, the average RMSD value of the Cα atoms of A2 protein relative to their initial positions fluctuated around 19 Å (Fig. 4b, lower panel). The dynamic movies for CG and AA simulations can be found online (Supplementary movies 1 and 2). Furthermore, we monitored the contact area between A2 and the lipids throughout the entire simulation trajectory. Impressively, the average contact area consistently remained stable, at ~1000 Å^2 (Fig. 4c). This observation serves as compelling evidence, indicating that the binding of A2 to the lipids is exceptionally stable during the AA simulations.

Subsequently, we proceeded to investigate the interaction mechanism between A2 and α5β1 integrin. We employed the blind docking method to predict the binding mode of A2 with α5β1 integrin, as illustrated in Fig. 4d. The most promising binding sites for A2 with α5β1 integrin were predicted to be located within the RGD-binding pocket. This pocket, previously identified at the center of a trench-like exposed surface on the top face of α5β1 integrin, is anticipated to be a key interaction site[39]. The A2's binding sites to α5β1 integrin and lipids were labeled as purple and red color, respectively (Fig. 4d). Surface hydrophobic potential (Fig. 4e1, e2) and electrostatic potential (Fig. 4e3, e4) analyses further provided molecular insights for these interactions. Between A2 and α5β1 integrin, hydrophobic interactions play an important role, evidenced by the frequent presence of non-polar residues such as Alanine in our analysis (Fig. 4e2). Between lipid surface and A2, our analysis revealed the critical role of α11 helix in A2, containing negatively charged residues such as D187, E189, D192, D194, D197, and D200. These residues are further attached to phospholipid head groups, which are locally polar and carry a slightly positive charge potential (Fig. 4e4).

To validate the proposed binding approach and its impact on transcytotic particle access, three complementary experiments were conducted. These experiments involved integrin knockdown at the EC receptor level, A2 mutation at the protein attachment level, and a "Zombie" experiment assessing active transportation. Through the transwell experiment, A2 pre-coating-induced augmentation of particle transcytosis across EC monolayer was significantly hindered upon the knockdown of α5 integrin in these cells (Fig. 4f). Two shRNA sequences (sh-ITGA5#1 and #2) that target the mRNA target were tested. EC integrity was not changed during the knockdown experimentation (Fig. S6). Moreover, we also utilized a transcytosis inhibitor genistein[40] to demonstrate the interference with A2-mediated LC-MSNP transcytosis. Our data indicated that more than 40% of particle transport was reduced in the HUVEC monolayer (Fig. S7).

Due to the crucial role played by residues D187, E189, D192, D194, D197, and D200 as depicted in Fig. 4e4, we introduced mutations in these six amino acid residues on A2, substituting them with alanine to reduce electrostatic interactions. The corresponding genes were synthesized by a core facility and integrated into the PET28a plasmid. The resulting A2 mutant protein (A2-M) was used to coat LC-MSNP. Both samples exhibited comparable size, PDI, and zeta potential values. However, an assessment of protein stability revealed that the A2-M coating resulted in reduced stability over time compared to the wild-type A2 coating. Additionally, microscale thermophoresis (MST)[41] analysis revealed K_d values of 7.93 nM for A2 and 30.88 nM for A2-M, respectively (Fig. S8). Furthermore, A2-M was utilized to pre-coat NIR-labeled LC-MSNP for a biodistribution study in orthotopic EMT6 tumor-bearing mice, in comparison to particles coated with wild-type (WT) A2. The effect of A2 coating was significantly compromised, resulting in a > 50% reduction in signal at the tumor site (Fig. 4g). Based on these findings, we attribute the reduced homing efficiency to the decreased binding stability during circulation, which likely impairs effective activation of α5β1 integrin and subsequent downstream signaling events.

As transcytosis is an energy-dependent process, we set up the "Zombie" model in EMT6 orthotopic tumor-bearing mice (Fig. S9), according to a published protocol[4]. Vascular fixation inhibited active particle transcytosis, while experimentally maintaining particle access through enlarged tumor fenestrations to the maximum extent possible[4,12]. We then used the "Zombie" mice to elucidate the impact of A2 pre-coating in the same BC model (Fig. 4h). After fixing the vasculature, the A2-coated F1 particles were circulated in a serum-containing solution for 2 h. The data illustrated the blocking effect on

https://doi.org/10.1038/s41467-025-61434-5

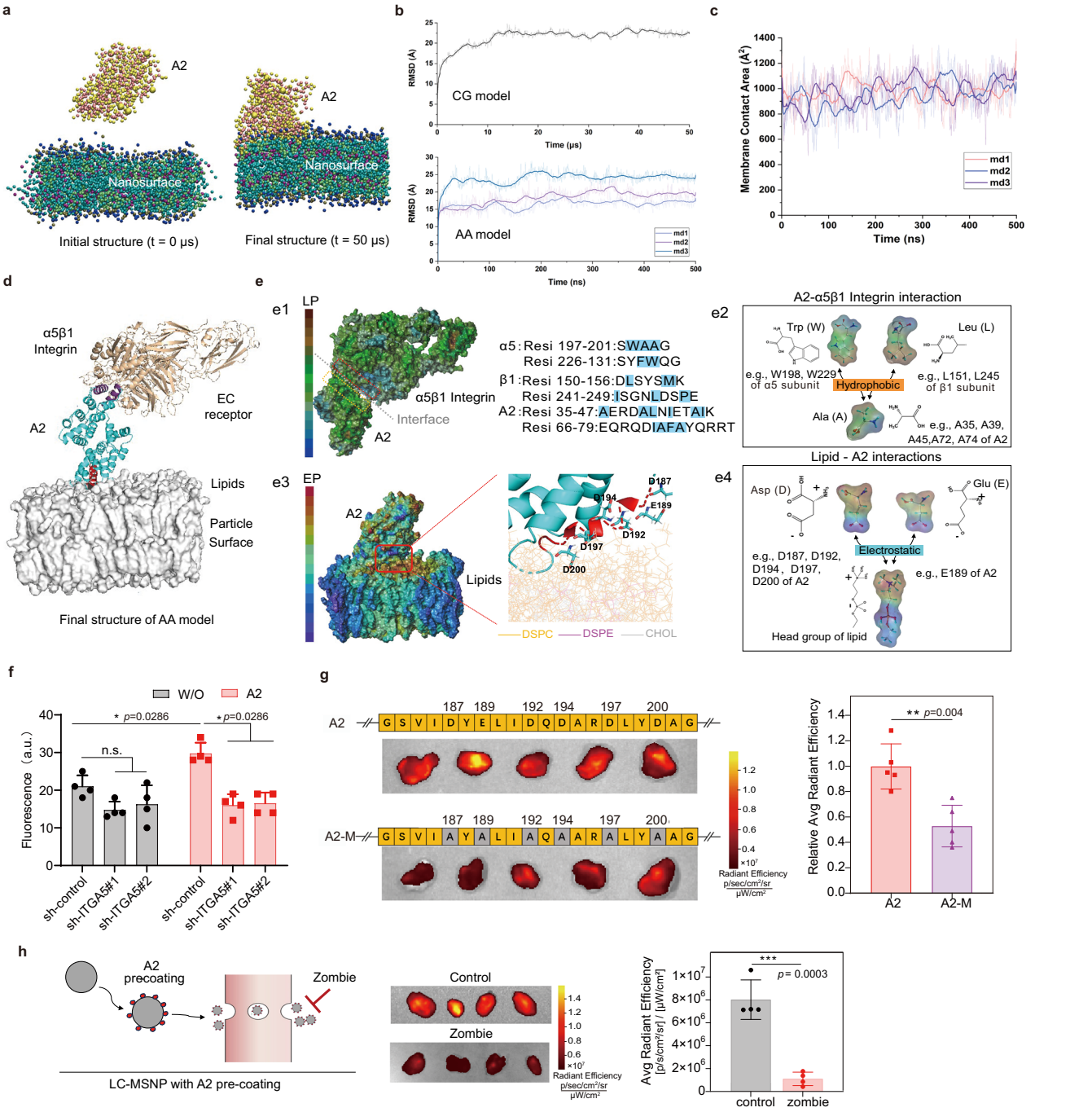

Fig. 4 | Mechanistic investigations on A2-mediated transcytosis enhancement. **a** The CG model's initial state (0 μs) showed random protein position and orientation relative to the lipid. After 50 μs of MD simulation with Martini force field, the equilibrated state was attained, characterized by protein adherence to the lipid membrane nano surface. **b** The Cα root mean square deviation (RMSD) of the protein concerning its initial positions within the CG model is depicted after 50 μs of simulation (upper panel) and further across three 500 ns simulations in the All-Atom (AA) model (lower panel). RMSDs were computed with backbone of protein alignment. **c** Time-Resolved contact area analysis illustrated the dynamic evolution of contact area between A2 and the lipid membrane over the entirety of the simulation. **d** Lipid surface-A2-α5β1 integrin interaction. Proteins are depicted in cartoon representation, with the lipid surface rendered in opaque gray. Notably, the α11 helix (red color) of A2 binds to the lipid, while helices (purple color) of A2 interact with α5β1 integrin. **e** While the interaction between A2 and α5β1 integrin was governed by hydrophobic interaction (**e1**), the interaction between A2 and nano surface (lipids) is mediated by electrostatic interaction (**e3**). The specific amino acids and their location in the indicated protein were demonstrated in the inserted boxes, **e2** (for A2 and α5β1 integrin) and **e4** (for A2 and lipids). **f** The HUVEC cell with integrin α5 subunit knockdown was detected by transwell for nanoparticle transcytosis assay ($n = 4$ independent experiments, two-tailed unpaired t test)). **g** We mutated six amino acid residues on A2, replacing them with alanine. The resulting A2 mutant (A2-M) was used to pre-coated particles with NIR labeling, followed by the nanoparticle distribution study in an orthotopic EMT6 mouse model. A2 coating was used as control ($n = 5$ mice, two-tailed unpaired t test)). **h** In the "zombie" mice, the blood vessels of EMT6 tumor-bearing mice were fixed, and a pump was employed to circulate blood containing A2-coated LC-MSNP. Data are depicted as mean ± SD. Statistical significance was evaluated *via* two-tailed unpaired t-test ($n = 4$ mice). Source data are provided as a Source Data file.

transcytosis, resulting in approximately 85% reduction for the A2-pre-coating effect. Moreover, the influence of A2 on particle enrichment in tumors was similarly diminished when treated with an α5β1 integrin inhibitor, ATN-161 (Fig. S10)[42].

Drawing from both in silico and the interference experimental data, our findings collectively demonstrated the essential role of lipid-A2-α5β1 interactions and nanoparticle transcytosis in the tumor vasculature system.

Pre-coating of A2 enhances the efficacy of drug delivery by in-house synthesized nanocarriers in PDAC and BC orthotopic models

Based on the above findings, we further hypothesized that it would be possible to use A2 pre-coating to improve the nanocarrier's efficacy through the activated transcytosis. Accordingly, we conducted a series of efficacy experiments in the PDAC and BC tumor models. As a proof-of-concept, we utilized our established remote loading approach to encapsulate DOX and IRIN, which are weak-base chemotherapeutic agents commonly prescribed for BC and PDAC[32,43]. Drug-laden LC-MSNP nanocarriers were fully characterized before use (Fig. 5a). In the first set of efficacy data, treatment was initiated ~10 days after orthotopic implantation of EMT6 BC cells. The EMT6 orthotopic tumor-bearing mice received IV injections of DOX-laden LC-MSNP nanocarriers with or without A2 pre-coating (DOX was 5 mg/kg; equivalent to A2 dose of ~2 mg/kg). Our results indicated that A2 pre-coating significantly enhanced the anti-BC effect of DOX LC-MSNP, with a p-value of 0.0165 (Fig. 5b). We also performed the efficacy study using IRIN LC-MSNP at an IRIN dose of 40 mg/kg, with or without the A2 coating. For IRIN LC-MSNP, A2 coating improved survival outcomes in the KPC orthotopic model, with a p value of 0.0035 (IRIN LC-MSNP vs A2 pre-coated IRIN LC-MSNP) (Fig. 5c). Please note that tumor burden in the KPC model was assessed using IVIS, which may be influenced by ascites at later stages[43,44] and is shown in Fig. S11.

Given that the A2 binding domain correlates with silica-supported lipid bilayer, we continued to hypothesize that the A2 pre-coating approach could improve the performance of liposomal formulations (non-supported lipid bilayer), potentially creating a broader impact on classic nanocarriers. Accordingly, we first repeated the electrophoresis experiment, which yielded results (Fig. 5d) highly similar to those depicted in Fig. 2d, thereby confirming our hypothesis about protein binding on the non-supported lipids abiotically. Accordingly, the second set of efficacy data is the anti-cancer effects in the EMT6 and KPC orthotopic model, with mice receiving in-house synthesized DOX-laden or IRIN-laden liposomes. A2 coating significantly enhanced the tumor-inhibitory efficacy of DOX liposomes, with a p-value of 0.0004 (Fig. 5e). Additionally, A2 coating improved overall survival rates compared to IRIN liposomes alone (log-rank test, $p = 0.0223$) (Fig. 5f).

Beyond the improvement in efficacy, it is important to thoroughly assess the safety of the A2 pre-coating approach to determine its suitability for use in nanotherapeutics. Body weight data from the efficacy studies in Fig. 5b, c, d, f, were provided as Fig. 5g, which demonstrated no major toxicity during the treatment. Since A2 targets the α5β1 integrin, we also investigated the expression of α5β1 integrin in ECs across the tumor and various organs, including the liver, heart, spleen, lung, kidney, and brain. While α5β1 integrin expression was abundant in liver endothelial cells, its levels in other organs were relatively low. (Fig. S12). Accordingly, the histological assessment revealed no significant abnormalities associated with the use of A2-coated nanocarriers (Fig. S13). This includes compatibility in the liver, likely due to its rapid metabolic activity and detoxification functions.

A2-mediated tumor access enhancement depends on α5β1 integrin expression in BC

We have demonstrated that the mechanism by which A2 pre-coating, facilitates transcytosis strongly depends on α5β1 integrins, with BC exhibiting the most significant increase in particle accumulation at the tumor site (Fig. 3c). This prompted us to revisit the EMT6 data, where we observed a significant but heterogeneous enhancement effect, resulting in a 4 ~ 9-fold increase (~6-fold on average) compared to particles without A2 pre-coating (Fig. 3c). This individual difference led to a follow-up investigation into how the level of α5β1 integrins influences the robustness of A2-mediated transcytosis. Accordingly, we replicated the A2 pre-coating effect in the orthotopic EMT6 model, studying mouse-to-mouse variation ($n = 12$). Additionally, we employed IF staining to assess the correlation between nanoparticle tumor accumulation and integrin α5β1 expression. A significant positive correlation was observed, with an R^2 value of 0.6456 (Figs. 5h and S14). To validate these findings, we repeated the experiment ($n = 7$) using flow cytometry to quantify the abundance of $\alpha5\beta1^+$ endothelial cells, with the gating strategy shown in Fig. S15. Consistently, the analysis revealed a similar correlation between nanoparticle accumulation and the population of $\alpha5\beta1^+CD31^+$ double-positive endothelial cells (Fig. S16).

We further obtained paired BC PDX models in immune-compromised NCG mice, from a PDX repository. These models were pre-characterized for fragments *per* kilobase per million (FPKM) information about ITGA5 (α5 subunit) and ITGB1 (β1 subunit). We intentionally selected BR00164 and BR00290 PDX models for their similar patterns in H&E staining and comparable degrees of stroma, as revealed by trichrome staining (Fig. S17). More importantly, the BR00164 model showed high expression of α5β1, whereas the BR00290 model exhibited low expression. The differential biodistribution results using liposomal- and LC-MSNP carriers in both models are summarized in Fig. 5i. Specifically, given the clinical prescription of liposomal DOX for BC management, both BR00164 and BR00290 models received single IV DOX liposomes with or without A2 pre-coating. Twenty-four hours post IV injection, tumor tissues were harvested to prepare tumor slices for DOX visualization (red fluorescence), CD31 immunofluorescent staining (in green), and nuclear staining (in blue). While A2 pre-coating exhibited a noticeable DOX fluorescence increase in the BR00164 model (α5β1 integrin high) (Fig. 5j, upper panel), the increase became negligible in the BR00290 model (α5β1 integrin low) (Fig. 5j, lower panel). Six randomly selected fields of view were analyzed for DOX's fluorescent intensity using ImageJ software (Fig. S18). We also replicated the PDX experiment, utilizing IV DOX-laden LC-MSNPs. In addition to the increased level of DOX fluorescence observed in the BR00164 model but not in the BR00290 model (Fig. S19), Si elemental analysis confirmed the differential biodistribution results (Fig. 5k). Please note that BR00164 exhibited slightly higher, though not statistically significant, accumulation compared to BR00290 when treated with DOX LC-MSNP without A2. This may be attributed to the ability of DOX LC-MSNP to bind endogenous Annexin A2, potentially enhancing tumor accumulation in BR00164 due to its higher expression of α5β1 integrin.

Use of A2 pre-coating to enhance the performance of approved and commercially available DOX liposome

Encouraged by the data generated using in-house nanocarriers, we sought to determine whether A2 pre-coating could similarly enhance the performance of commercial liposomes. To make a rational choice, we first synthesized a series of LC-MSNP model nanoparticles with varying PEG densities (0–8%). These particles were incubated with A2 and subjected to gentle shaking to facilitate A2 attachment. The results showed that A2 pre-coating was effective across all PEG densities (Fig. S20). We also assessed the stability of A2 attachment on LC-MSNPs with low (0%) and high (3%) PEG. Notably, A2 coating remained highly stable on the 3% PEG particles for 48 h, while A2 attachment decreased by ~50% on LC-MSNPs without PEG. We surmise that this difference is due to the higher "surface accessibility" in low-PEG samples, which may result in weaker protein retention on the surface. This

https://doi.org/10.1038/s41467-025-61434-5

a

NPs	Size（nm）	PDI
IRIN liposome	141.0	0.132
A2 pre-coating IRIN liposome	195.5	0.142
IRIN LC-MSNP	164.7	0.095
A2 pre-coating IRIN LC-MSNP	184.6	0.081
DOX liposome	94.8	0.166
A2 pre-coating DOX liposome	105.8	0.088
DOX LC-MSNP	143.5	0.083
A2 pre-coating DOX LC-MSNP	188.5	0.085

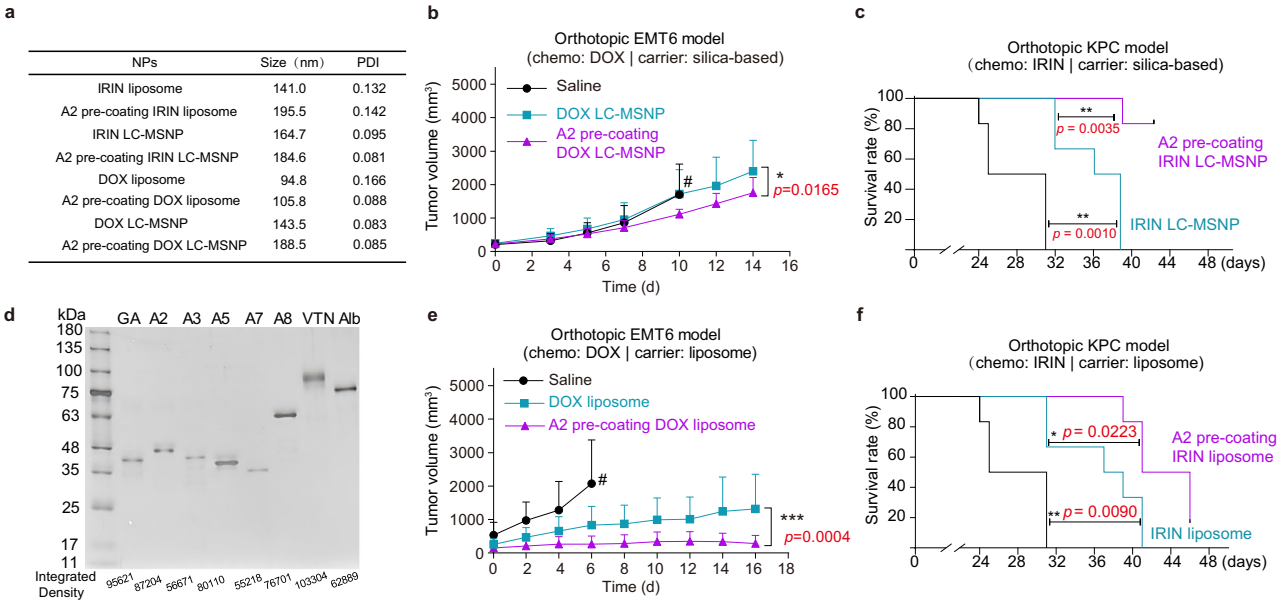

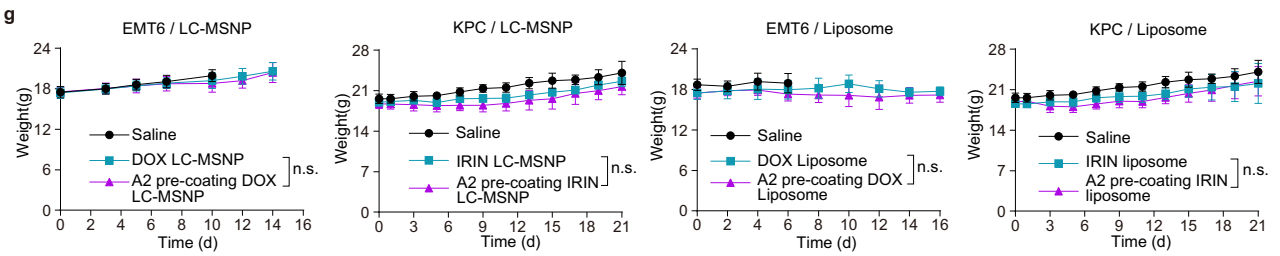

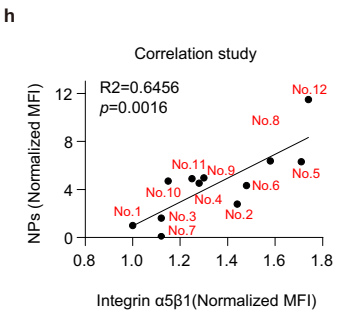

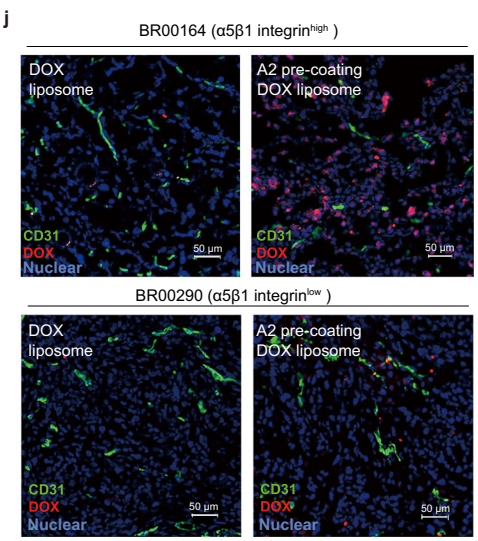

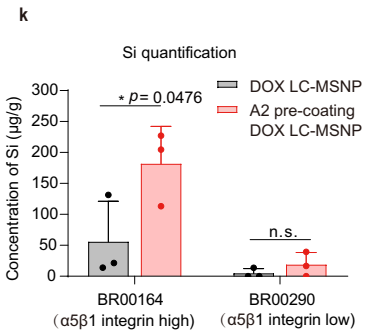

i

PDX features			Signal Intensity (AU, liposome)			Signal Intensity (AU, silica-based)		
PDX models	Integrin α5 / β1	Predicted Responsiveness	DOX liposome	A2 pre-coating DOX liposome	Fold increase	DOX LC-MSNP	A2 pre-coating DOX LC-MSNP	Fold increase
BR00164	20.5 / 9.5	Responsive	0.071 ± 0.036	1.502 ± 0.356	21.1x $p = 0.0025$	0.0493 ± 0.036	0.764 ± 0.119	15.5x $p = 0.0002$
BR00290	4.1 / 4.0	Non-responsive	0.218 ± 0.090	0.266 ± 0.166	1.2x n.s.	0.039 ± 0.012	0.033 ± 0.008	0.85x n.s.

reduced stability of A2 coating likely contributes to the diminished coating effect observed in the absence of PEG (Fig. S21).

For treating BC and PDAC patients, the most frequently prescribed nanomedicines include Myocet® (non-Peglated DOX liposome), commercial PEGylated DOX liposome (such as Duomeisu®, which is a generic Doxil® and contains 5% PEG), and Onivyde® (IRIN liposome that contains 0.3% PEG). Myocet®, non-PEGylated DOX liposome with circulatory half-life of 16.4 h in patients[45], is not prioritized due to the potential risk of "A2 falling" during circulation, even if an efficient protein attachment at very beginning. Onivyde®, which has 0.3% PEG, is not prioritized as the top choice because it did not fall into the favorable zone in terms of PEG density and A2 binding stability. We decided on the prioritized testing of 5% PEGylated DOX liposome (with the brand name of Duomeisu®) in the BC model in vivo. This liposome

Fig. 5 | A2 pre-coating enhances drug delivery efficacy of LC-MSNP and liposome. a Size and PDI of drug-laden nanocarriers before and after A2 coating were fully characterized. **b**, **c** DOX- and IRIN-laden LC-MSNPs were used to treat orthotopic EMT6 BC and KPC PDAC, respectively. A2-pre-coated carriers were IV injected twice per week, with controls involving drug-laden LC-MSNP and saline. Kaplan–Meier analysis suggested that A2 pre-coating improved the efficacy of IRIN LC-MSNP in PDAC ($n = 6$ mice, log-rank testing). Similar improvement was observed in EMT6 BC model ($n = 9$ ~ 10 mice, two-tailed paired t-test). **d** We confirmed the abiotic A2 binding effect using liposome ($n = 3$ independent experiments). **e**, **f** In-house synthesized liposomal carriers were loaded with IRIN and DOX. The treatment schedule was similar to (**b**, **c**). The dose for IRIN and DOX were 40 mg/kg and 10 mg/kg, respectively. A statistically significant efficacy enhancement was evident using A2-pre-coated DOX-loaded liposome in EMT6 orthotopic model ($n = 5$ ~ 6 mice, two-tailed paired t-test), while survival outcome was enhanced by A2 pre-coated IRIN liposome in PDAC, demonstrated by Kaplan–Meier analysis ($n = 6$ mice, log-rank testing). #: Observation was terminated due to animal welfare reason. **g** Body weight data in the efficacy data in the **b**, **c**, **e**, and **f** (two-tailed unpaired *t* test). Please note that the animal study assessing IRIN-loaded LC-MSNPs and liposomes was conducted concurrently, and thus both groups share the same saline control. For clarity, we have plotted the data according to the carrier type. **h** Demonstration of A2-mediated particle access increase depends on α5β1 integrin expression in the EMT6 tumor-bearing mice. **i** We selected BR00164 PDX with high α5β1 integrin expression and BR00290 PDX with low α5β1 integrin expression to compare A2-mediated transcytosis activation. The table summarizes the major PDX features and differential biodistribution outcome using DOX-laden liposomal- or LC-MSNP nanocarriers in both PDX models ($n = 3$ mice). **j** PDX mice received DOX liposome w/wo A2 coating. CD31 staining (green) was performed, followed by confocal imaging of blood vessels and DOX. **k** Similar experiment was repeated using DOX LC-MSNP, followed by Si elemental analysis. Data are depicted as mean ± SD ($n = 3$ mice, two-tailed unpaired *t* test). Source data are provided as a Source Data file.

was selected because it contains the optimal PEG% for A2 binding and stability.

To mimic the clinical practice, we first developed a bedside preparation protocol (Fig. 6a), wherein A2 solutions are mixed with commercial DOX liposome and incubated at 37 °C for one hour before IV injection. The as-purchased DOX liposome and its A2 pre-coating formulation were fully characterized before use (Fig. 6b). This included the electrophoresis experiment confirming efficient A2 binding on the commercial DOX liposome (Fig. 6c). The A2-coated commercial DOX liposomes were well dispersed in serum-supplemented saline and exhibited colloidally stable for at least 0 ~ 48 h (Fig. 6d). Importantly, both uncoated and A2-coated liposomes released less than ~0.1% free DOX when incubated in serum-supplemented saline at 37 °C for 24 h (Fig. 6e).

Pharmacokinetic (PK) studies were performed on BALB/c mice using A2-coated commercial DOX liposomes, with the uncoated commercial DOX liposomes serving as the control (DOX, 5 mg/kg). Both uncoated and A2-coated liposomes exhibited similar PK profiles (Fig. 6f). The half-lives ($t_{1/2}$) for the commercial DOX liposomes and A2-coated DOX liposomes were 23.9 and 20.26 h, respectively. Additionally, key PK parameters, including area under the curve (AUC) and clearance, were comparable for both formulations, indicating that A2 coating has minimal impact on the systemic PK of the commercial DOX liposomes (Fig. 6g).

We further assessed the therapeutic enhancement of the A2 pre-coating strategy using commercial DOX liposomes in an orthotopic EMT6 model. Tumor-bearing mice received IV injections of A2-coated or uncoated DOX liposomes (DOX: 5 mg/kg; A2: ~1.25 mg/kg) every four days for a total of five doses (Fig. 6h). A2 pre-coating significantly enhanced the anti-cancer efficacy of the commercial DOX liposomes in vivo (Fig. 6i, j, $p = 0.0014$). Remarkably, we also observed significantly improved survival outcomes in the A2 coating group ($p = 0.0056$). Notably, two out of eight mice achieved long-term survival, extending to 80 days post-treatment (Fig. 6k).

Discussion

Growing evidence suggests that the ATR effect, which includes transcytosis, may not depend on vascular leakiness and could play a dominant role in the nano drug delivery in stroma-rich solid tumors[3,4,14,15]. Through analysis of protein attachment, we identified A2 modification as a convenient means of activating tumor transcytosis and improving the efficacy of nanocarriers in solid tumors. Annexin A2 is a calcium-dependent phospholipid-binding protein that plays a significant role in various cellular processes, including membrane trafficking, endocytosis, and exocytosis[46]. By targeting A2 or utilizing it as a molecular bridge, we were able to improve the specificity and efficiency of drug delivery in PDAC and BC. From a materials science perspective, A2 and its derivatives can be engineered as an interfacial functional modulating material (IFMM), designed for efficient bio-barrier penetration among other functions (*e.g.* nanomachine-enabled access). This includes the implementation of ETR (Enhanced Transcytosis and Retention), a mechanism distinct from the classical EPR effect, enabling tumor access without relying on enlarged tumor fenestration[14]. Although the A2 pre-coating technology demonstrated potency, we did not observe significant particle access to the brain in our case (Fig. S22). Additionally, we have shown that the introduction of the A2 coating does not promote toxicity, including undesirable tumor progression (Fig. S23). Furthermore, safety assessments have demonstrated that A2 coating is non-toxic to major organs, including those expressing α5β1. Regarding the expression of α5β1, the divergent results observed in BC PDX data suggest the feasibility of considering a predictive approach to achieve robust efficacy enhancement for nanocarriers. We also wish to highlight that A2-mediated enhanced transcytosis could have broad implications for IV-injected nanocarriers. In addition to the PEG density, we conducted a comparative study using A2-coated LC-MSNPs with core sizes ranging from 50 nm to 150 nm. Notably, all LC-MSNPs within this size range effectively attached to A2 (Fig. S24a). A similar enhancement of A2 uptake at the tumor site was observed (Fig. S24b). Additionally, we also investigated the impact of various physiological and pathological conditions, including age, immunological suppression, and inflammation status, on the A2 pre-coating effect in mice. In vivo data revealed no significant differences across these states (Figs. S25 and 26).

We also want to briefly comment on the limitations of our work. While the surface attachment of intact A2 is experimentally functional, further optimization and simplification may still be necessary. One potential approach is to simplify A2 as A2-derived peptide or fragment that could be used to enhance the nanocarrier's performance. Moreover, developing in situ analytical techniques to track the fate of the A2 coating would provide new insights into its stability, interactions, and performance in biological environments, enabling optimization for targeted therapeutic delivery.

Methods

Materials

Tetraethyl orthosilicate (TEOS), Triethanolamine (TEA-oL), cetyl trimethyl ammonium bromide (CTAC) and (3-aminopropyl) triethoxysilane (APTES) were purchased from Aladdin, China. Trisodium citrate and $HAuCl_4 \cdot 3H_2O$ were purchased from Macklin, China. 1,2-Distearoyl-sn-glycero-3-phosphocholine (DSPC), 1,2-distearoyl-sn-glycero-3-phospho-ethanol amine-N-[methoxy(polyethylene glycol)-2000] (ammonium salt) (DSPE-PEG2000), cholesterol (Chol), 1,2-dioleoyl-sn-glycero-3-phosphate (DOPA), and (2,3-Dioleoyloxy-propyl)-trimethylammonium-chloride (DOTAP) were purchased from SunLipo Nanotech, China. Dylight 680 (Dy680) NHS ester was purchased from Thermofisher. The annexin family proteins and GAPDH were

https://doi.org/10.1038/s41467-025-61434-5

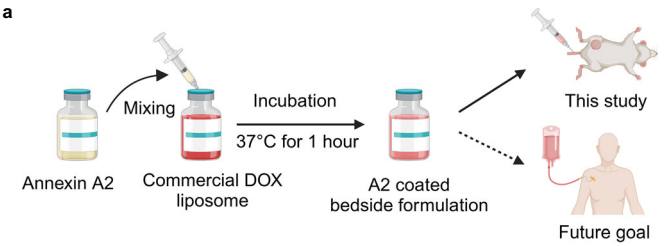

b

Formulation	Size (nm)	PDI	ζ-potential (mV)
Commercial DOX liposome	83.52±0.50	0.067±0.021	-4.45±0.99
A2 pre-coating commercial DOX liposome	84.65±0.69	0.042±0.009	-7.00±1.52

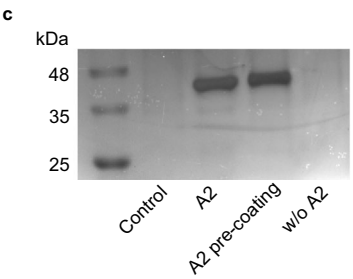

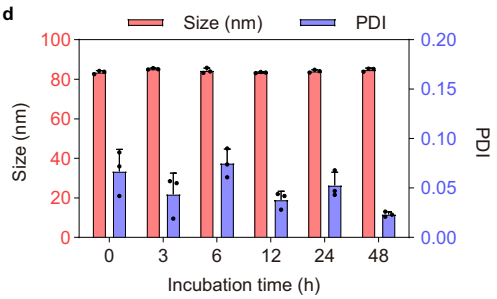

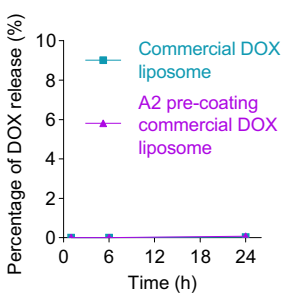

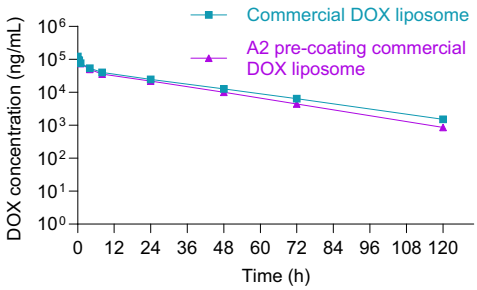

g

	$t_{1/2}$ (h)	AUC_{0-t} (10^6 μg/L•h)	$AUC_{0-\infty}$ (10^6 μg/L•h)	V (L/kg)	CL (L/h/kg)
Commercial DOX liposome	23.90±1.87	1.88±0.091	1.93±0.10	0.089	0.0027
A2 pre-coating commercial DOX liposome	20.26±0.76	1.61±0.075	1.64±0.077	0.089	0.0030

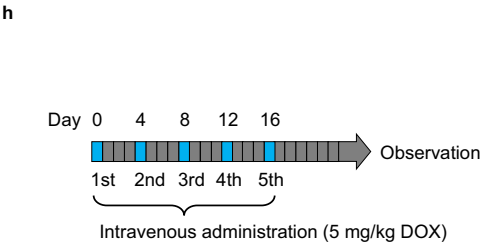

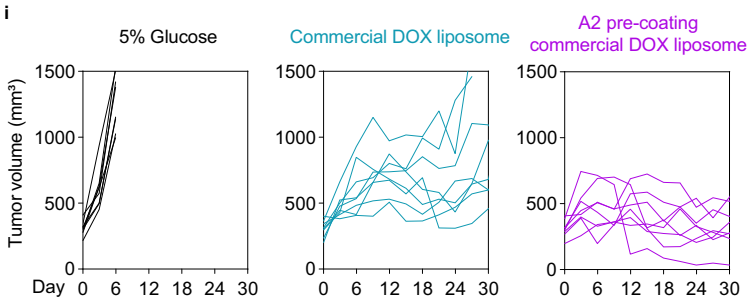

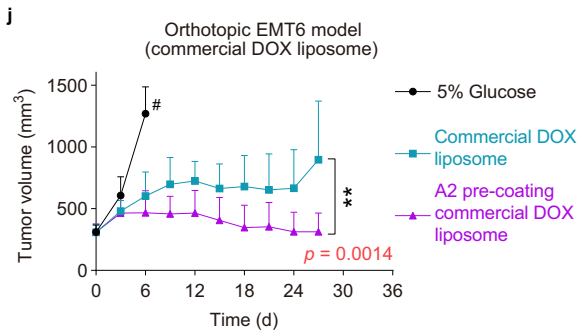

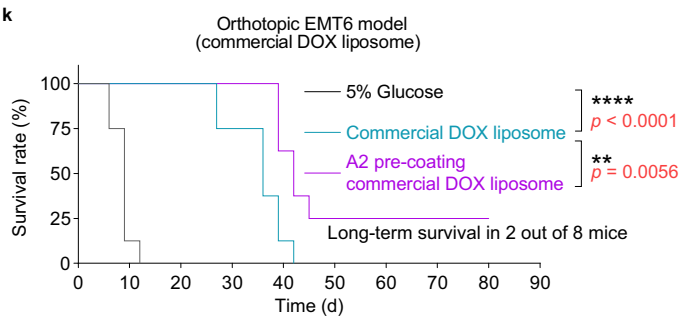

purchased from Solarbio, China. The vitronectin was purchased from Sino Biological, Inc. The luciferin potassium bioluminescent substrate was purchased from PerkinElmer, Inc. The ATN-161 was purchased from Selleck, China. The Precast-Gel (4–20%) and the PAGE Gel Silver Staining Kit were purchased from Solarbio, China. Penicillin, streptomycin, Dulbecco's modified Eagle medium (DMEM), RPMI 1640, and Fetal bovine serum (FBS) were purchased from Wisent, China. Antibodies (integrin α5/103805, CD31/102414, CD45/103155) were purchased from Biolegend, USA.

Nanoparticle synthesis

Synthesis of bare MSNPs. Thirty-six milliliters of CTAC (25 wt% in ddH_2O) were gently added to 684 mL ddH_2O with stirring at 480 rpm. The solution was then heated to 85 °C, and 2.88 g of triethanolamine in 16 mL ddH_2O was added. After 30 min of heating and stirring, 24 mL of TEOS was gently added, followed by stirring and heating for an additional 3 h. The suspension naturally cooled to room temperature, and approximately 500 mL of ethanol was added to precipitate the silica particles. To eliminate CTAC, the suspension was centrifuged at

Fig. 6 | A2 coating enhances the anti-tumor efficacy of commercial DOX liposome in vivo. a Scheme of A2 coating on commercial DOX liposome (*Created in BioRender. Meng, H. (2025)* https://BioRender.com/sqvm0zp). **b** Size, PDI and zeta potential of commercial DOX liposome w/wo A2 coating ($n = 3$ independent experiments). **c** A2 protein can be efficiently attached on the commercial DOX liposome ($n = 3$ independent experiments). **d** Size and PDI values of A2 pre-coating commercial DOX liposome were measured in serum-supplemented saline at different time points ($n = 3$ independent experiments). **e** Drug release profiles of commercial DOX liposome w/wo A2 coating when incubated with serum-supplemented saline ($n = 3$ independent experiments). **f** Comparative PK studies in mice using IV injection of commercial DOX liposome w/wo A2. **g**, PK parameters were calculated using DAS 2.0 software. **h** A2 pre-coating commercial DOX liposome was IV injected every 4 days, with control involving commercial DOX liposome without A2 coating for a total 5 dosages. The dose for DOX was 5 mg/kg. **i** Spaghetti curves of each treated animals from day 0–30. **j** A statistically significant efficacy enhancement was evident using A2-pre-coated FDA-approved and commercial DOX liposome, compared to as-purchased liposome in EMT6 orthotopic model ($n = 8$ mice, two-tailed paired t test, $^{**}p = 0.0014$). #: Observation was terminated due to animal welfare reason. **k** Based on Kaplan–Meier analysis and log-rank testing, we observed significantly improved survival outcomes w/wo A2 pre-coating ($^{**}p = 0.0056$). Data are shown as mean ± SD. Source data are provided as a Source Data file.

14,000 × *g* for 10 min twice, followed by three washes using acidic ethanol (HCl/ethanol, 2%, v/v) at 14,000 × *g* for 35 min each. To remove residual HCl, two additional washes with pure ethanol were performed at 14,000 g for 35 min each.

Lipid coating on silica surface. To achieve distinct surface charges on nanoprobes, as illustrated in Fig. 1, we utilized various lipid mixtures to form the lipid coat on the MSNP surface. The formulations were outlined in Fig. 1. Briefly, a mixture of 20 mg/mL of MSNP in PBS and 0.5 mg/μL of the lipid mixture (in ethanol, twice the mass of MSNP) was heated to 65 °C. Subsequently, the MSNP suspension was added to the lipid solution and probe-sonicated with an ultrasonic homogenizer. The resulting nanoparticles were carefully washed with PBS to remove excess ethanol and stored in PBS. These processes generated three particle types, designated as F1 ~ F3, which were subsequently subjected to protein identification analysis (see below).

Synthesis of an Au core-labeled silica probe. For ease of TEM visualization, we synthesized an alternative version of LC-MSNP incorporating a gold (Au) core. To synthesize an ~10 nm Au core, 110 mL of 1 mM $HAuCl_4$ was brought to a boil with vigorous stirring. Subsequently, 10.9 mL of a 38.8 mM trisodium citrate aqueous solution was rapidly added, leading to a final solution color of burgundy. The growth of the MSNP shell on the Au core was accomplished using a previously reported method[3] with slight modifications. Further lipid coating was achieved as described above.

Preparation of drug-loaded LC-MSNP or liposome. While the identification of the A2 protein will be introduced later, it will suffice for now to describe the preparation of the drug-loaded nanocarriers. Accordingly, we synthesized DOX-loaded formulations to treat EMT6 breast cancer and IRIN-loaded nanocarriers to treat KPC orthotopic PDAC. DOX and IRIN are the first-line options for these cancer types. The synthesis of these materials was previously reported by us using a trapping agent-mediated approach[32,43]. While TEA_8SOS served as the trapping agent in the IRIN formulation, $(NH4)_2SO_4$ was used for DOX loading.

Characterization

All nanoparticles were thoroughly characterized prior to biological use. The hydrodynamic diameter and zeta potential of the specified nanoparticles were measured using DLS (NanoBrook 90PlusPALS, USA). For protein-coated nanocarriers (see below), protein adsorption was confirmed by SDS-PAGE analysis. Particle size and polydispersity index (PDI) were monitored at designated time points to assess colloidal stability. Drug loading for each formulation was quantified prior to use.

Identification of protein attachment on F1 ~ F3 nanoparticles

To mimic the protein attachment on nano surface in vivo, blood plasma was obtained from KPC tumor-bearing mice and centrifuged at 4 °C, 1000 × *g* for 5 min to eliminate hemocytes. The separation and identification of protein species were designed based on a published protocol with minor modification[33,34]. Subsequently, 50 μL of 1 mg/mL F1 ~ F3 nanoparticles were incubated with 200 μL of plasma for 3 h at 37 °C on a shaker. The mixture was then centrifuged for 45 min at 14,000 × *g*, 4 °C, to separate the particles from the supernatant. Loosely attached proteins were removed by resuspending the particles in 500 μL of 10× PBS, followed by centrifugation at 4 °C, 14,000 × *g* for 45 min, repeated three times. The firmly attached proteins were extracted using lysis buffer (6 M guanidine hydrochloride, 50 mM Tris, 20 mM TCEP, 50 mM IAA), followed by sonication at 4 °C for 1 min and incubation in the dark for 40 min. The lysates were then boiled for 5 min, and nanoparticles were separated by centrifugation. The resulting lysates were treated with Lys-C (Promega Corporation, Madison, USA) at a ratio of 1:100 for 4 h at 37 °C. The digestion mixture was subsequently diluted with 25 mM NH_4HCO_3, followed by overnight incubation with trypsin (Promega Corporation, Madison, USA) at 37 °C. Finally, peptides were acidified, desalted using C18 resin, and freeze-dried.

Peptides were chromatographically separated on a 20 cm reversed-phase capillary emitter column (100 μm, 5 μm Venusil XBP C18 resin, Agela Technologies, China) and analyzed using the Q Exactive instrument from Thermo Fisher Scientific. Peptides were loaded in a 0.2% (v/v) formic acid solution and eluted with a nonlinear 80-min gradient of 5–30% buffer B (0.1% (v/v) formic acid, 90% (v/v) acetonitrile) at a flow rate of 300 nL/min. The full MS scan targeted a value of 3×10^6 in the range of m/z 320–1700, with a maximum injection time of 20 ms and a resolving power of 70,000 at m/z 200. MS raw files underwent processing using MaxQuant software (version 1.4.1.2) with a label-free quantification workflow (MaxLFQ). The peak lists were searched using the mouse Uniprot FASTA with reversed protein sequences and a common contaminants database using the Andromeda search engine. Peptides with at least six amino acids were considered for identification, and the false discovery rate for both peptides and proteins was set at 1%.

Protein pre-coating on nanoparticle surface

Two types of materials, namely liposomes and LC-MSNP, were employed in this project. Briefly, 50 μL of a 1 mg/mL nanoparticle solution was incubated with 100 μL of a 0.5 mg/mL pure protein solution. The tested proteins included A2, A3, A5, A7, A8, and VTN, with GAPDH and albumin serving as reference proteins. To ensure sufficient coating efficiency, the incubation time was set to 1 hour with gentle vibration. The diameter and zeta potential of the coated samples were characterized by DLS (NanoBrook 90PlusPALS, USA). Particle-coated proteins were further analyzed by SDS-PAGE. The particles were dispersed in 150 μL of 62.5 mM Tris-HCl supplemented with 2 wt% SDS and incubated for 15 min at 90 °C to facilitate the desorption of proteins from LC-MSNP or liposome. For SDS-PAGE analysis, the desorbed protein solution was combined with 1× SDS denaturant and incubated for an additional 5 min at 90 °C. Subsequently, the samples were applied onto a commercial gel (PG42010, Solarbio, China) with 4–20% polyacrylamide and subjected to electrophoresis for 50 min at 150 V. Finally, the protein bands were visualized using a PAGE Gel Silver Staining Kit following the manufacturer's instructions.

Cell lines

4T1, EMT6, PyMT-derived Py8119, CT26, and HUVEC cells were obtained from the American Type Culture Collection (ATCC) or the

China Center for Type Culture Collection. KPC cells were derived from a spontaneous PDAC tumor in a transgenic *Kras*$^{LSL\text{-}G12D/+}$*Trp53*$^{LSL\text{-}R172H/+}$*Pdx1-Cre* mouse. All eukaryotic cell lines used in this study were authenticated by STR assay, and routinely tested for mycoplasma contamination using a PCR-based assay. These tests are performed every ~3 months, and all cell lines were confirmed to be mycoplasma-free during the study period.

Nanoparticle transwell assay

HUVEC cells were seeded on the upper surface of the membrane in rat tail collagen-coated polycarbonate Transwell inserts (No. 3401 Costar; Corning; 0.4 μm pore size; 12 mm diameter) with a density of 5×10^5 cells *per* well. The medium in both upper and basal compartments was changed with fresh DMEM medium every day, and cells were cultured for 4–6 days until a confluent monolayer was formed. The barrier integrity of the monolayer was monitored by measuring cell permeability to 70 kDa FITC-dextran before the experiment. After confirming the restriction of paracellular transport, 200 μl DMEM medium (with 10% FBS) containing nanoparticles coated with different proteins (150 μg/mL) was added to the upper chamber of the insert, and the medium of the basal side was replaced with 0.5 mL medium. After 24 h, the entire volume of the basal well was removed, and the concentration of the nanoparticles was examined by measurement of NIR fluorescence (excitation wavelength at 660 nm and emission wavelength at 700 nm).

MD simulations

All the MD simulations were performed with the computer software, GROMACS 2018.4. The lipid components, including DSPC, DSPE and CHOL were setup using Coarse-Grained model for saving equilibration time, with a composition ratio of 58: 3: 39. The A2 protein structure was obtained from the Protein Data Bank (PDB, http://www.rcsb.org/pdb) (PDB entry 1w7b). The atomistic structures were then coarse-grained using an insane file adapting Martini coarse-graining method. The CG system was pre-equilibrated in a water box of $10 \times 10 \times 16$ nm^3 with Martini2.2 force field. After a 20,000,000-step energy minimization, the system was equilibrated in the NPT ensemble for 50 μs. The long-range electrostatics was calculated by the reaction-field method. The van der Waals interaction and Coulomb interaction were considered within 1.1 nm. The v-rescale method and Berendsen method were used to maintain the system temperature at 310 K and pressure at 1.0 bar, respectively. The pressure coupling was isotropic. The coupling time constants for both the pressure and temperature were set to 1.0 ps. When the system reached the equilibration, the CG model was converted into an all-atom model, which was continued to proceed MD simulation for a further 500 ns until the system reached a completely converged state. The RMSD calculation was carried out by first aligning the system by the Cα atoms of the A2 protein, and then the RMSD was calculated using the Cα atoms of the A2 with respect to their initial positions in the aligned simulation system. The A2 protein-lipid bilayer contact area was calculated using the Gromacs command 'gmx sasa'.

Docking analysis

The blind docking was performed using ZDOCK 3.0.2 through ZDOCK Server website (https://zdock.umassmed.edu) to investigate the binding site of α5β1 integrin with A2. The structure of α5β1 integrin was downloaded from the PDB database (PDB entry 3vi4). The top 10 complex structures were selected to analyze the binding sites of α5β1 integrin with A2. The lipophilic and electrostatic potentials of the integrin, A2 and lipid bilayer were displayed by SYBYL-X 1.2. The detailed residues were displayed by the open-source software Pymol.

Syngeneic tumor models

Orthotopic PDAC model. Under aseptic conditions, a 0.7 cm incision was made on the left flank of C57BL/6 J mice (6–8 week-old, female, were purchased from Charles River, China). One million KPC-luc cells in 100 μL PBS/Matrigel (1:1 v/v) were injected into the pancreatic tail. The fascial layers and the skin were closed using absorbable sutures. Tumors were grown for ~4 weeks, and the success of KPC-luc orthotopic xenografts was assessed through IVIS imaging. The animal model was characterized using H&E or Trichrome staining before use.

Orthotopic breast cancer model. The 4T1 (5×10^5 cells in 50 μL PBS), EMT6 (3×10^6 cells in 50 μL PBS/Matrigel, 1:1 v/v), and PyMT-derived Py8119 (1×10^6 cells in 50 μL PBS/Matrigel, 1:1 v/v) cells were injected into the left 4th mammary fat pad of 6-week-old female Balb/c mice (6–8 week-old, female, were purchased from Charles River, China). For the biodistribution study, tumors were grown for 3 weeks to reach a volume of ~0.8 cm^3. For the efficacy study in the EMT6 orthotopic model, treatment commenced 10 days after implantation, corresponding to a tumor size of 0.2 cm^3.

Orthotopic colon cancer model. CT26 cells were first subcutaneously inoculated into female BALB/c mice. Once tumors were established, mice were euthanized, and tumors were sectioned into 2×4 mm pieces in saline. The tumor chunk was implanted orthotopically. Briefly, a 2-cm incision was made in the abdomen of female BALB/c mice to expose the cecum and its cecal pouch. Subsequently, the cecum wall was gently injured with a sterile scalpel, and the tumor block was affixed to the injury site using sutures. The fascial layer and skin were then closed using absorbable sutures.

Biodistribution study

To compare the best-performing nanoparticle in vivo, multiple rounds of biodistribution studies were conducted in this work. Generally, 0.1 % Dy680 dye-labeled nanoparticles were IV injected into mice bearing various tumors (e.g., KPC, 4T1, EMT6, etc.) at a particle dose of 50 mg/kg. Ex vivo imaging of the tumor and major organs (heart, lungs, spleen, liver, and kidneys) was carried out 24 h post-injection. Quantitative analysis of fluorescent ROIs was performed using LivingImage software (version 4.3.1, PerkinElmer).

Mechanistic transcytosis studies

Ultrastructural TEM visualization. Orthotopic tumor-bearing mice were treated by IV injection of Au-labeled A2 pre-coated F1 nanoparticle at a dose of 100 mg/kg. Tumor biopsies were obtained 24 h post-treatment, washed in PBS, and promptly fixed at 4 °C using 2.5% glutaraldehyde. Subsequent sample preparation and sectioning were carried out by Tianjin Bairuisi Biotechnology Co., Ltd. After fixation in 1% OsO_4, the samples were dehydrated in propylene oxide and embedded in resin. Tissue slices (60 to 80 nm in thickness) were placed on copper grids and viewed under a JEOL 1200-EX electron microscope.

α5β1 knockdown study using HUVEC cells. The psPAX2, pMD2.G, and pLL3.7 lentiviral packaging system was used to obtain the α5β1 knockdown HUVEC cells, using the methods of lentiviral packaging and cell infection. The shRNA sequences used in the experiments were as follows: shRNA-1: TGGACAAGGCTGTGGTATA, shRNA-2: GAGAGGAGCCTGTGGAGTA. The resulting α5β1 knockdown HUVEC cells were used to repeat the transwell study, with a view to demonstrating the critical role of α5β1 integrin in the "sandwich" mechanism.

"Zombie" model. As one of the experimental approaches to study transcytosis in vivo, we investigated the effect of A2-mediated particle tumor access by utilizing "Zombie" mice[4]. The blood of EMT6 tumor-bearing mice was initially collected via transcardiac perfusion with a PBS solution containing sodium heparin (1 mg/mL). Whole mice were then fixed by transcardiac perfusion with a fixative solution (4% formaldehyde and 0.5% glutaraldehyde in 1× PBS) for 1 hour. The fixative

was subsequently washed out by perfusion with PBS for 20 min. To simulate the blood environment, nanoparticles were introduced into the collected mouse blood. A peristaltic pump circulated the nanoparticle solution at a physiologically relevant flow rate (5–7 mL/min) within the fixed mice, maintaining circulation for 2 h. Afterward, nanoparticles were cleared from the blood vessels by perfusion with PBS. Tumors were excised from these mice and imaged by IVIS. As a control, live mice were IV injected with the same blood concentration of nanoparticles. After 2 h, blood was cleared by cardiac perfusion, tumors were removed, and IVIS imaging was performed to analyze nanoparticle enrichment.

A2 mutation study. We utilized mutated A2 to demonstrate the compromised enhancement of tumor access in the EMT6 model. Following calculations to determine the binding site (D187, E189, D192, D194, D197, D200) of A2 to phospholipid-based particles, we aimed to validate this binding mechanism by introducing mutations in six amino acid residues on A2, substituting them with alanine. Tsingke Biotechnology Co., Ltd. synthesized the corresponding genes, which were then integrated into the PET28a plasmid. Protein expression and purification were subsequently conducted by Beijing Catascis Biotech Co., Ltd. A2 mutant protein (A2-M) was used to generate comparative data as compared to protein coating using WT A2.

Correlation study between integrin abundance and A2 coating outcome

To investigate the potential correlation between integrin expression and A2-mediated tumor access, A2-pre-coated Dy680-labeled LC-MSNP were IV injected into orthotopic EMT6 tumor-bearing mice at a dose of 50 mg/kg ($n = 12$). 24 h post-injection, the mice were sacrificed, and the tumors were embedded in OCT and cryosectioned into 6 μm slices. IF staining for integrin was performed. The distribution of integrin and Dy680-labeled nanoparticles was analyzed by confocal microscopy. In a separate experiment ($n = 7$), we performed a parallel study using flow cytometry and IVIS imaging in place of IF staining to quantify integrin expression and nanoparticles accumulation within the tumor.

The results from the EMT6 model prompted us to advance our study using a patient-derived tumor xenograft (*PDX*) model. Due to the logistical limitations of the PDX model, we conducted a focused repetition of the essential aspects of the biodistribution study. This aimed to illustrate the differential enhancing outcomes achieved by employing A2 pre-coating in both silica- and liposomal-based formulations for breast cancer. Briefly, the preparation of PDX models, the administration of treatment, and sample collection were conducted by a commercial service. The selected PDXs were pre-characterized for integrin expression. 6–8 weeks female NCG mice were inoculated with patient-derived breast cancer cells BR0164 (high α5β1 integrin expression) and BR0290 (low α5β1 integrin expression). Tumor volume and body weight of PDXs were measured weekly. When the average tumor volume reached approximately 600–800 mm^3, each PDX model was randomly divided into four groups based on tumor volume and body weight. The groups were administered with DOX liposome, A2 pre-coating DOX liposome, DOX LC-MSNP, and A2 pre-coating DOX LC-MSNP. Tumor tissues and organs were collected 24 h after IV injection. The tumors were embedded in OCT and then frozen sectioned. IF staining for CD31 was performed, and the distribution of DOX and blood vessels was imaged by confocal microscopy. For the use of silica-based formulation, tumor tissues were further tested for Si elemental analysis using ICP-MS in the National Institute of Metrology of China.

Efficacy enhancement using in-house nanocarriers in PDAC and BC models

Ten days post-KPC-luc tumor implantation, mice carrying the tumors were randomly divided into five groups ($n = 6$). Each group received IV injections of 100 μL of the following formulations: IRIN liposome, IRIN LC-MSNP, A2 pre-coating IRIN liposome, and A2 pre-coating LC-MSNP, at an IRIN dose equivalent of 40 mg/kg, twice per week for a total of 6 administrations. Saline served as the negative control. Similarly, 10 days post EMT6 tumor implantation, the breast cancer bearing mice received IV injections of 100 μL of different formulations: DOX liposome, DOX LC-MSNP, A2 pre-coating DOX liposome, and A2 pre-coating DOX LC-MSNP, at a DOX dose equivalent of 10 mg/kg for liposome carrier, and 5 mg/kg for LC-MSNP carrier, twice per week for a total of 5 administrations. Saline was used as a negative control. Since the therapeutic dose may vary between different carrier types, we empirically used a lower chemotherapy dose for LC-MSNP, as they potentially offer more efficient drug delivery compared to liposomes[43]. IVIS imaging was used to monitor the KPC orthotopic tumor burden weekly. Since a limitation using IVIS in measuring orthotopic GIT tumors that carry a luciferase reporter gene is the potential interference from the presence of ascites at the later stage of the experiment, the survival outcome was recorded in KPC-luc orthotopic model[43,44]. The tumor size of EMT6 orthotopic tumors was measured by a caliper. The statistical analysis of the differences between different groups was performed using t-test and log-rank (Mantel-Cox) test (Graphpad Prism software, vesion 8.4). Moreover, we conducted an acute toxicity assessment in mice receiving the A2-pre-coated nanocarriers, such as evaluations of body weight and major organ histology using H&E staining.

Efficacy enhancement of commercial DOX liposomes (Duomeisu®)

Bedside preparation protocol. 78.1 μL A2 solution (3.2 mg/mL) was mixed with 500 μL commercial DOX liposome (Duomeisu®, CSPC Pharmaceutical Group Co, 2 mg/mL) and incubated at 37 °C for one hour. The mixture was diluted to a final DOX concentration of 1 mg/mL using 5% Glucose before IV injection.

Pharmacokinetics study. BALB/c female mice ($n = 3$ per group) received a single IV injection of A2-coated or uncoated commercial DOX liposomes at a DOX equivalent dose of 5 mg/kg. Blood samples (~50 μL) were collected at specified time points (2 min, 15 min, 30 min, 1 h, 4 h, 8 h, 24 h, 48 h, 72 h and 120 h) via murine orbital vascular plexus into heparinized 1.5 mL tubes. The blood samples were centrifuged at 400 × *g* and 4 °C for 10 min to obtain plasma. The plasma samples were subsequently analyzed by LC-MS/MS for DOX quantification. Specifically, chromatographic separation was performed on Agilent 1100 high-performance liquid chromatograph system (Agilent Technologies, USA) using Inertsustain Swift C18 column (2.1 × 50 mm, 5.0 μm) with an in-line filter at 40 °C. The injection volume was 5 μL for plasma samples and 10 μL for tube samples. The mobile phases were 10% acetonitrile containing 0.1% formic acid (A) and 90% acetonitrile containing 0.1% formic acid (B), which were used in a gradient elution method at a total flow rate of 0.40 mL/min as following: 0–0.40 min, 20%–100% B; 0.40–2.50 min, 100% B; 2.50–2.51 min, 100%–20% B; 2.51–3.50 min, 20% B. The high-performance liquid chromatograph system was coupled to an API 4000 triple quadrupole mass spectrometry (AB SCIEX LLC, USA) equipped with an electrospray ionization (ESI) source and operated under the positive multiple reaction monitoring (MRM) mode. The ion source related parameters were set as following: CUR: 30 Psi, CAD: 6 Psi, ISV: 5500 V, TEM: 550 °C, GAS1: 50 Psi, GAS2: 50 Psi. Quantification was performed using Anlyst1.6.2 software (AB SCIEX LLC, USA). Pharmacokinetic parameters were calculated using DAS 2.0 software.

Efficacy enhancement. A2-pre-coated or uncoated commercial DOX liposome was IV injected into orthotopic EMT6 tumor-bearing mice ($n = 8$ per group) every 4 days for a total of 5 dosages at a DOX equivalent dose of 5 mg/kg. The negative control group was treated with 5% glucose. The tumor size was measured by a caliper. Statistical

analysis of the differences between groups was performed using a paired *t* test and a log-rank (Mantel–Cox) test.

Ethics statement

All animal studies were conducted in accordance with the Guide for the Care and Use of Laboratory Animals and approved by the Institutional Animal Care and Use Committee of the National Center for Nanoscience and Technology (NCNST21-21065-0608). In accordance with our approved animal welfare guideline, animals must be euthanized if the tumor mass is estimated to exceed 10% of the animal's body weight. For example, in a 25 g mouse, the maximum allowable tumor diameter is 20 mm. At no point did the tumor burden exceed these approved limits. The PDXs used in this study were established from surgical tumor specimens obtained from breast cancer patients. The collection and use of patient samples were approved by the IRB under protocol number 202412101335000491097.

Statistics and reproducibility

Tumor growth curve data were analyzed using a two-tailed paired Student's t-test, while mice survival rate curves were analyzed by Kaplan–Meier analysis and log-rank testing. Other data were analyzed using a two-tailed unpaired Student's t-test. The above statistical analyses were performed using GraphPad Prism (version 8.4), and data are presented as mean ± SD. When $p < 0.05$, the data were considered to be statistically significant. All experiments conducted in this study included all samples and data points without any exclusions. The in vivo experimental samples were randomly grouped, and all in vitro experiments were conducted at least three times independently to ensure the reliability and reproducibility of the results.

Reporting summary

Further information on research design is available in the Nature Portfolio Reporting Summary linked to this article.

Data availability

The data supporting the findings of the study are included in the main text and supplementary information files. Source data are provided with this paper. The mass spectrometry proteomics data have been deposited to the ProteomeXchange Consortium via the PRIDE[47] partner repository (http://www.ebi.ac.uk/pride) with the dataset identifier PXD063915. The MD simulation and docking analysis data have been provided as Supplementary Data 1. Source data are provided with this paper.

References

1. Fang, J., Nakamura, H. & Maeda, H. The EPR effect: unique features of tumor blood vessels for drug delivery, factors involved, and limitations and augmentation of the effect. *Adv. Drug Deliv. Rev.* **63**, 136–151 (2011).
2. Nakamura, Y., Mochida, A., Choyke, P. L. & Kobayashi, H. Nanodrug delivery: is the enhanced permeability and retention effect sufficient for curing cancer?. *Bioconjug. Chem.* **27**, 2225–2238 (2016).
3. Liu, X. et al. Tumor-penetrating peptide enhances transcytosis of silicasome-based chemotherapy for pancreatic cancer. *J. Clin. Invest.* **127**, 2007–2018 (2017).
4. Sindhwani, S. et al. The entry of nanoparticles into solid tumours. *Nat. Mater.* **19**, 566–575 (2020).
5. McNeil, S. E. Evaluation of nanomedicines: stick to the basics. *Nat. Rev. Mater.* **1**, 16073 (2016).
6. Zhou, Q. et al. Enzyme-activatable polymer-drug conjugate augments tumour penetration and treatment efficacy. *Nat. Nanotechnol.* **14**, 799–809 (2019).
7. Ikeda-Imafuku, M. et al. Strategies to improve the EPR effect: a mechanistic perspective and clinical translation. *J. Control. Release* **345**, 512–536 (2022).
8. Liu, X., Jiang, J. & Meng, H. Transcytosis - an effective targeting strategy that is complementary to "EPR effect" for pancreatic cancer nano drug delivery. *Theranostics* **9**, 8018–8025 (2019).
9. Meng, H. et al. Use of a lipid-coated mesoporous silica nanoparticle platform for synergistic gemcitabine and paclitaxel delivery to human pancreatic cancer in mice. *ACS Nano* **9**, 3540–3557 (2015).
10. Nel, A., Ruoslahti, E. & Meng, H. New insights into "permeability" as in the enhanced permeability and retention effect of cancer nanotherapeutics. *ACS Nano* **11**, 9567–9569 (2017).
11. Tylawsky, D. E. et al. P-selectin-targeted nanocarriers induce active crossing of the blood-brain barrier via caveolin-1-dependent transcytosis. *Nat. Mater.* **22**, 391–399 (2023).
12. Dasgupta, A., Sofias, A. M., Kiessling, F. & Lammers, T. Nanoparticle delivery to tumours: from EPR and ATR mechanisms to clinical impact. *Nat. Rev. Bioeng.* **2**, 714–716 (2024).
13. Ji, Y. et al. Use of ratiometrically designed nanocarrier targeting CDK4/6 and autophagy pathways for effective pancreatic cancer treatment. *Nat. Commun.* **11**, 4249 (2020).
14. Qin, M., Feng, Z. & Meng, H. Enhanced transcytosis and retention (ETR) effect. *Sci. Bull.* **69**, 3640–3643 (2024).
15. Kingston, B. R. et al. Specific endothelial cells govern nanoparticle entry into solid tumors. *ACS Nano* **15**, 14080–14094 (2021).
16. Iannotta, D., A, A., Kijas, A. W., Rowan, A. E. & Wolfram, J. Entry and exit of extracellular vesicles to and from the blood circulation. *Nat. Nanotechnol.* **19**, 13–20 (2024).
17. Nance, E. Intracerebral fate of engineered nanoparticles. *Nat. Nanotechnol.* **19**, 273–274 (2024).
18. Ruoslahti, E. Access granted: iRGD helps silicasome-encased drugs breach the tumor barrier. *J. Clin. Invest.* **127**, 1622–1624 (2017).
19. Yang, A. C. et al. Physiological blood-brain transport is impaired with age by a shift in transcytosis. *Nature* **583**, 425–430 (2020).
20. Xiao, W. et al. The protein corona hampers the transcytosis of transferrin-modified nanoparticles through blood-brain barrier and attenuates their targeting ability to brain tumor. *Biomaterials* **274**, 120888 (2021).
21. Kucharz, K. et al. Post-capillary venules are the key locus for transcytosis-mediated brain delivery of therapeutic nanoparticles. *Nat. Commun.* **12**, 4121 (2021).
22. Yang, D. et al. Transferrin functionization elevates transcytosis of nanogranules across epithelium by triggering polarity-associated transport flow and positive cellular feedback loop. *ACS Nano* **13**, 5058–5076 (2019).
23. Quader, S., Kataoka, K. & Cabral, H. Nanomedicine for brain cancer. *Adv. Drug Deliv. Rev.* **182**, 114115 (2022).
24. Miller, M. A. et al. Predicting therapeutic nanomedicine efficacy using a companion magnetic resonance imaging nanoparticle. *Sci. Transl. Med.* **7**, 314ra183 (2015).
25. Biancacci, I. et al. Monitoring EPR effect dynamics during nanotaxane treatment with theranostic polymeric micelles. *Adv. Sci.* **9**, e2103745 (2022).
26. Tarn, D. et al. Mesoporous silica nanoparticle nanocarriers: biofunctionality and biocompatibility. *Acc. Chem. Res.* **46**, 792–801 (2013).
27. Ashley, C. E. et al. The targeted delivery of multicomponent cargos to cancer cells by nanoporous particle-supported lipid bilayers. *Nat. Mater.* **10**, 389–397 (2011).
28. Fang, W. et al. Complex roles of annexin A2 in host blood-brain barrier invasion by cryptococcus neoformans. *CNS Neurosci. Ther.* **23**, 291–300 (2017).
29. Na Pombejra, S., Salemi, M., Phinney, B. S. & Gelli, A. The metalloprotease, Mpr1, engages annexinA2 to promote the transcytosis of fungal cells across the blood-brain barrier. *Front. Cell. Infect. Microbiol.* **7**, 296 (2017).

30. Boj, S. F. et al. Organoid models of human and mouse ductal pancreatic cancer. *Cell* **160**, 324–338 (2015).
31. Feng, Z. et al. Efficient nano-enabled therapy for gastrointestinal cancer using silicasome delivery technology. *Sci. China Chem.* **64**, 1946–1957 (2021).
32. Liu, X. et al. Irinotecan delivery by lipid-coated mesoporous silica nanoparticles shows improved efficacy and safety over liposomes for pancreatic cancer. *ACS Nano* **10**, 2702–2715 (2016).
33. Blume, J. E. et al. Rapid, deep and precise profiling of the plasma proteome with multi-nanoparticle protein corona. *Nat. Commun.* **11**, 3662 (2020).
34. Baimanov, D. et al. In situ analysis of nanoparticle soft corona and dynamic evolution. *Nat. Commun.* **13**, 5389 (2022).
35. Nonaka, M. et al. Overcoming the blood-brain barrier by Annexin A1-binding peptide to target brain tumours. *Br. J. Cancer* **123**, 1633–1643 (2020).
36. Wu, M. H., Ustinova, E. & Granger, H. J. Integrin binding to fibronectin and vitronectin maintains the barrier function of isolated porcine coronary venules. *J. Physiol.* **532**, 785–791 (2001).
37. Ciregia, F. et al. Modulation of $\alpha_V\beta_6$ integrin in osteoarthritis-related synovitis and the interaction with $VTN_{(381\text{-}397\ a.a.)}$ competing for TGF-β1 activation. *Exp. Mol. Med.* **53**, 210–222 (2021).
38. Du, R. et al. Downregulation of annexin A3 inhibits tumor metastasis and decreases drug resistance in breast cancer. *Cell Death Dis.* **9**, 126 (2018).
39. Nagae, M. et al. Crystal structure of α5β1 integrin ectodomain: atomic details of the fibronectin receptor. *J. Cell Biol.* **197**, 131–140 (2012).
40. Tuma, P. & Hubbard, A. L. Transcytosis: crossing cellular barriers. *Physiol. Rev.* **83**, 871–932 (2003).
41. Romain, M., Thiroux, B., Tardy, M., Quesnel, B. & Thuru, X. Measurement of protein-protein interactions through microscale thermophoresis (MST). *Bio Protoc.* **10**, e3574 (2020).
42. Slack, R. J., Macdonald, S. J. F., Roper, J. A., Jenkins, R. G. & Hatley, R. J. D. Emerging therapeutic opportunities for integrin inhibitors. *Nat. Rev. Drug Discov.* **21**, 60–78 (2022).
43. Liu, X. et al. Improved efficacy and reduced toxicity using a custom-designed irinotecan-delivering silicasome for orthotopic colon cancer. *ACS Nano* **13**, 38–53 (2019).
44. Terracina, K. P. et al. Development of a metastatic murine colon cancer model. *J. Surg. Res.* **199**, 106–114 (2015).
45. Makwana, V., Karanjia, J., Haselhorst, T., Anoopkumar-Dukie, S. & Rudrawar, S. Liposomal doxorubicin as targeted delivery platform: current trends in surface functionalization. *Int. J. Pharm.* **593**, 120117 (2021).
46. Gerke, V., Creutz, C. E. & Moss, S. E. Annexins: linking Ca2+ signalling to membrane dynamics. *Nat. Rev. Mol. Cell Biol.* **6**, 449–461 (2005).
47. Perez-Riverol, Y. et al. The PRIDE database at 20 years: 2025 update. *Nucleic Acids Res.* **53**, D543–D553 (2025).

Acknowledgements

This work was supported by National Key Research and Development Program of China (2022YFA1207300, 2021YFA1200902), National Natural Science Foundation of China (32201143, 32271452, and 82204300), and the Strategic Priority Research Program of the Chinese Academy of Sciences (XDB36000000). X.L. is thankful for National Natural Science Fund for Excellent Young Scientist Fund Program (Overseas) and the startup funding support from Zhejiang Cancer Hospital, Hangzhou Institute of Medicine (HIM), Chinese Academy of Sciences (CAS). H.M. thanks the startup packages of National Center for Nanoscience and Technology, and CAS Innovation team science award.

Author contributions

H.M. performed conceptualization, supervision, data analysis, manuscript writing and funding acquisition; Y.L. and Q.W. performed experiments and contributed to data analysis; J.J., Z.F., Z.Z., and T.R. contributed to some experiments; M.Q. and X.L. contributed to the data analysis; Y.L.Z. and C.J.B. contributed to the data discussion and revised the manuscript.

Competing interests

The authors declare no competing interests.

Additional information

Supplementary information The online version contains supplementary material available at https://doi.org/10.1038/s41467-025-61434-5.

Correspondence and requests for materials should be addressed to Huan Meng.

Peer review information *Nature Communications* thanks the anonymous reviewer(s) for their contribution to the peer review of this work. A peer review file is available.